J|A|C|S
JOURNAL OF THE AMERICAN CHEMICAL SOCIETY

Article

pubs.acs.org/JACS

Structural and Spectroscopic Features of Mixed Valent $Fe^{II}Fe^{I}$ Complexes and Factors Related to the Rotated Configuration of Diiron Hydrogenase

Chung-Hung Hsieh,[†] Özlen F. Erdem,[‡] Scott D. Harman,[†] Michael L. Singleton,[†] Edward Reijerse,[‡] Wolfgang Lubitz,*[,‡] Codrina V. Popescu,*[,§] Joseph H. Reibenspies,[†] Scott M. Brothers,[†] Michael B. Hall,*[,†] and Marcetta Y. Darensbourg*[,†]

[†]Department of Chemistry, Texas A&M University, College Station, Texas 77843, United States
[‡]Max Planck Institute for Chemical Energy Conversion, Stiftstrasse 34-36, 45470 Muelheim a.d. Ruhr, Germany
[§]Department of Chemistry, Ursinus College, Collegeville, Pennsylvania 19426, United States

Supporting Information

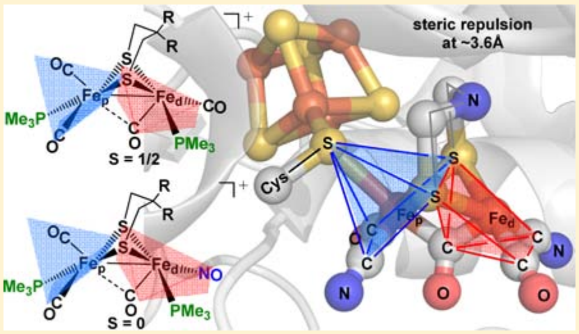

ABSTRACT: The compounds of this study have yielded to complementary structural, spectroscopic (Mössbauer, EPR/ENDOR, IR), and computational probes that illustrate the fine control of electronic and steric features that are involved in the two structural forms of $(\mu\text{-SRS})[Fe(CO)_2PMe_3]_2^{0,+}$ complexes. The installation of bridgehead bulk in the $-SCH_2CR_2CH_2S-$ dithiolate (R = Me, Et) model complexes produces 6-membered FeS_2C_3 cyclohexane-type rings that produce substantial distortions in $Fe^{I}Fe^{I}$ precursors. Both the innocent (Fc^+) and the noninnocent or incipient (NO^+/CO exchange) oxidations result in complexes with inequivalent iron centers in contrast to the $Fe^{I}Fe^{I}$ derivatives. In the $Fe^{II}Fe^{I}$ complexes of $S = 1/2$, there is complete inversion of one square pyramid relative to the other with strong super hyperfine coupling to one PMe_3 and weak SHFC to the other. Remarkably, diamagnetic complexes deriving from isoelectronic replacement of CO by NO^+, $\{(\mu\text{-SRS})[Fe(CO)_2PMe_3]\ [Fe(CO)(NO)PMe_3]^+\}$, are also rotated and exist in only one isomeric form with the $-SCH_2CR_2CH_2S-$ dithiolates, in contrast to R = H (Olsen, M. T.; Bruschi, M.; De Gioia, L.; Rauchfuss, T. B.; Wilson, S. R. *J. Am. Chem. Soc.* **2008**, *130*, 12021−12030). The results and redox levels determined from the extensive spectroscopic analyses have been corroborated by gas-phase DFT calculations, with the primary spin density either localized on the rotated iron in the case of the $S = 1/2$ compound, or delocalized over the $\{Fe(NO)\}$ unit in the $S = 0$ complex. In the latter case, the nitrosyl has effectively shifted electron density from the $Fe^{I}Fe^{I}$ bond, repositioning it onto the spin coupled Fe−N−O unit such that steric repulsion is sufficient to induce the rotated structure in the $Fe^{II}\text{-}\{Fe^{I}(^{\bullet}NO)\}^8$ derivatives.

INTRODUCTION

The structurally unique diiron catalytic unit Figure 1 that exists in the active site of the [FeFe]-H_2ase (known as the H-cluster) is of special interest to biomimetic/synthetic chemists as its construction exploits diatomic CO and CN^- ligands rather than typical donors covalently bound to a peptide chain.[1−3] Thus, the light atom to atom torsion angles responsible for the mismatch of donor ligand−metal geometric preferences that are expected to account for high rates of catalysis in classical transition-metal biocatalysts are minimal in such organometallics.[4−6] Furthermore, the ease of modifying a simple precursor that has the Fe_2S_2 core of the [FeFe]-H_2ase enzyme active site and the possibility to develop base metal catalysts for fuel cell use have attracted a new coterie of chemists to biomimetic synthesis.[7,8] They bring the spectroscopic tools and structure/bonding approaches of organometallic chemistry to bear on defining the primary differences between the active site and the $(\mu\text{-}S(CH_2)_3S)[Fe(CO)_3]_2$ parent model, Figure 1. Despite the simplicity of the latter, modifications abound that

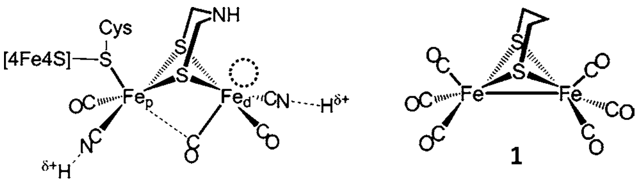

Figure 1. (Left) The enzyme active site of [FeFe]-hydrogenase showing the unique, "rotated" geometry.[1−3] (Right) Structure of the parent model complex, $(\mu\text{-pdt})[Fe(CO)_3]_2$, complex **1**, pdt = propane dithiolate.[10]

Received: May 18, 2012
Published: July 10, 2012

dx.doi.org/10.1021/ja304866r | *J. Am. Chem. Soc.* 2012, 134, 13089−13102

lead to closer analogues of the active site diiron unit. They include positioning a bridgehead amine for proton shuttling in the S to S linker as is found in the active site[9] and exchange of CO for cyanide.[10−12] Even the pendant 4Fe4S cluster has been reproduced in a more complete model of the 6Fe6S, H_2-producing cluster; analogues of this redox active pendant are also achievable.[13,14]

The major geometrical distinction between the natural and synthetic units displayed in Figure 1 is as follows: The well-known $(\mu\text{-RS})_2[Fe(CO)_2L]_2$ and $(\mu_2\text{-S-R-S})[Fe(CO)_2L]_2$ molecules are symmetrical and best defined as two square pyramids (SP) edge-bridged by thiolate sulfurs; apical ligands in each SP, typically a CO, are pointed outward. The underside of the edge-bridged SPs is rich in electron density, comprising an Fe−Fe bond derived from the spin-coupled d^7, Fe^I units (Fe--Fe = ca. 2.5 Å).[15] The 2Fe2S subsite of the active site can be similarly described; however, one SP is inverted with respect to the other. This gives an apparent open site on the iron that resides underneath the bridgehead amine, designated as Fe_d, the iron distal to the 4Fe4S cluster in Figure 1, a positioning that is indicative of a proton-shuttling role for the amine nitrogen in the H_2 heterolysis/heterogenesis reaction mechanism ($H_2 = H^+ + H^- = 2H^+ + 2\ e^-$).[16] Trans to that site, the apex of the "rotated" or inverted SP is a semibridging carbonyl in the as-isolated, oxidized redox level of the protein that becomes less semibridging, perhaps linear, in the reduced form.[17] This iron is designated Fe_p, which is proximal to the 4Fe4S cluster.

As the first example of such a structure in organometallic chemistry, the unusual nature of the [FeFe]-H_2ase active site was initially described (by one of us) as "entatic",[3] assuming the protein matrix enforced the rotated conformer in contrast to the symmetrical structures that are isolated on the chemists' benchtops. In fact, it has become apparent that the stable and isolable, mixed-valent paramagnetic species that exists within the H_{ox} state is, while heretofore unknown, synthetically accessible and reproduced in certain one-electron oxidized species that are constructed as inspired by the [FeFe]-H_2ase active site, vide infra.[18−20]

The composition of the active site provides indication of the hydrogenase catalytic mechanism. Computational mechanistic studies of the enzyme have been augmented by electrochemical studies of the synthetic analogues, concluding that the optimal catalytically active conformation is the rotated structure.[21−23] In the $Fe^{II}Fe^{II}$ oxidized state an open site on Fe_d^{II} is disposed toward H_2 binding with heterolytic cleavage ensuing. In the reduced Fe^IFe^I or $Fe^{II}Fe^0$ state, access to electron density on reduced Fe_d by a proton, shuttled in by the strategic amine base, results in oxidative addition with conversion to a terminal $Fe_p^{II}Fe_d^{II}$-H, subject to subsequent H^+/e^- addition and H_2 production. As opposed to a bridging hydride, the advantages of a terminal H^- and η^2-H_2 complex at an Fe^{II} center are well established;[24,25] however, access to synthetic analogues of the rotated structure is challenging, particularly in the reduced state.

Many of the hundreds of synthetic analogues of the [FeFe]-H_2ase active site based on the simple $(\mu\text{-S}(CH_2)_3S)[Fe(CO)_3]_2$, $(\mu\text{-pdt})[Fe(CO)_3]_2$, complex **1**, as parent precursor are solution electrocatalysts for H_2 production[26] and others have advanced synthetic approaches to immobilization or attachment to carbon electrodes or photodevices.[27−29] Thus far, only a few have displayed a reversible Fe^IFe^{II} redox couple and yielded to one-electron chemical oxidation with isolation of a mixed-valent complex; examples of these are given in Figure 2. The features of these complexes include the presence of two or more ligands that are better donors than CO, steric bulk built into the second coordination sphere, such as the aryl groups in complexes **A** or **B**,[18,19] or the bridgehead carbon substituents of complex **C**,[20] and the SP/inverted-SP, or rotated, geometry. In analogy to the active site, we have labeled the open face iron as Fe_d and the pseudo-octahedral iron as Fe_p.

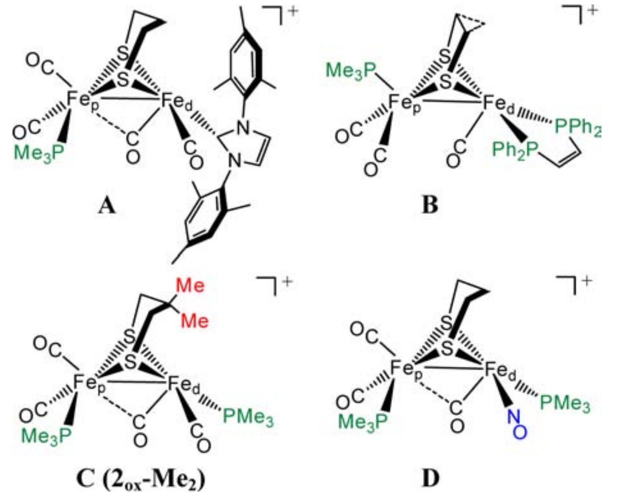

Figure 2. (**A**−**C**) Mixed-valent $Fe^{II}Fe^I$ model complexes with geometries similar to the [FeFe]-hydrogenase active site.[18−20] (**D**) Nitrosyl derivative of [FeFe]-hydrogenase model complex in basal/basal conformation.[30]

Another class of rotated structures was reported by the Rauchfuss group in 2008;[30] the replacement of a CO by NO^+ yielded isomeric forms of the diiron complexes. The major isomer was largely isostructural with its symmetrical precursor, while the minor one demonstrated a structural change, rendering a largely rotated structure, complex **D**. Studies of complex **D** were hampered by interconversions between isomers, including phosphine ligand positional isomers, and the NO vs CO as bridging diatomic ligand. Hence, we have endeavored to connect our steric bulk strategies for the stabilization of the mixed-valent Fe^IFe^{II} rotated complexes, shown as **A** and **C** in Figure 2, with the CO/NO^+ substituted derivatives described by the Rauchfuss group.[30] In this pursuit, we have encountered an Fe^IFe^I complex that is significantly "rotated" in the solid state and another stable one-electron oxidized, mixed-valent, $S = 1/2$, $Fe^{II}Fe^I$ complex with a rotated structure. With the aid of bridgehead steric pressure the NO^+/CO exchange derivative cleanly yielded a rotated $S = 0$, $Fe_p\{Fe_d(^\bullet NO)\}$ complex. Full characterization, including computational, EPR/ENDOR, and Mössbauer studies delineate the balance of metal−metal bond order vs μ-CO stabilization of such dithiolate-bridged diiron organometallics. Extensive spectroscopic studies (high-field Mössbauer) are reported separately.[31]

■ RESULTS AND DISCUSSION

The precursors to the diiron complexes explored in this study, $(\mu\text{-SCH}_2CR_2CH_2S)[Fe(CO)_3]_2$, R = Me and Et, complexes **1-Me₂** and **1-Et₂**, as well as the parent $(\mu\text{-S}(CH_2)_3S)[Fe(CO)_3]_2$ complex **1**, display nearly identical band patterns and positions in their solution ν(CO) IR spectra, indicating no influence of the bridgehead substitution on electron density at iron, as reported by the CO ligands.[32] Ligand exchange of CO with PMe_3 occurs stepwise for **1-Me$_2$** and **1-Et$_2$**, requiring harsher conditions for the second substitution and with concomitant changes in the ν(CO) IR spectra as expected for addition of the better donor ligands. Whereas the solution IR spectra overlay well for the (μ-$SCH_2CR_2CH_2S$)[$Fe(CO)_2PMe_3$]$_2$, R = Me and Et, complexes **2-Me$_2$**[20] and **2-Et$_2$**, respectively, a difference is noted in the solid state IR spectra (Supporting Information, Figure S1), relating to disparities in the molecular structures as described below.

Dark red crystals of **2-Et$_2$** were obtained from MeOH solution and subjected to X-ray diffraction analysis. Shown in Figure 3 are views of **2-Me$_2$** (from data reported earlier)[20] and **2-Et$_2$**. Both find the PMe_3 ligands in basal transoid positions and both show distortions from the largely symmetrical edge-bridged SP structures observed for all-CO analogues, **1-Me$_2$** and **1-Et$_2$**.[32] Steric hindrance from the bridgehead substituents impose a 29° staggering of the apical carbonyls for **2-Me$_2$**, whereas the 75° $(OC)_{ap}$−Fe−Fe′−$(CO)_{ap}'$ torsion angle signifies **2-Et$_2$** is almost entirely in the rotated form with one CO in an apparent semibridging position. On further analysis of the metric data, Supporting Information (Table S1), a major difference is seen between the computed τ-values[33] for individual pentacoordinate Fe derived from structures of complexes **1-Me$_2$** and **1-Et$_2$** vs those of **2-Me$_2$** and **2-Et$_2$**. These contain almost perfect square pyramids with τ values close to zero for both irons. One iron of complex **2-Me$_2$**, the iron related to Fe_p of the active site, Figure 1, is likewise in a SP environment; however, the second has some trigonal bipyramidal character (τ = 0.37; for ideal TBP, τ = 1).[33] In complex **2-Et$_2$** there is TBP character associated with both iron centers, with the Fe_d τ value = 0.68. As viewed from the side, the CO group that largely rests underneath the Fe−Fe bond vector deviates only slightly from linearity, with $\angle_{Fe-C-O}$ = 172°. There is a slight increase in Fe−Fe distance in the PMe_3 derivatives of 0.04 to 0.07 Å as compared to the all-CO analogues.

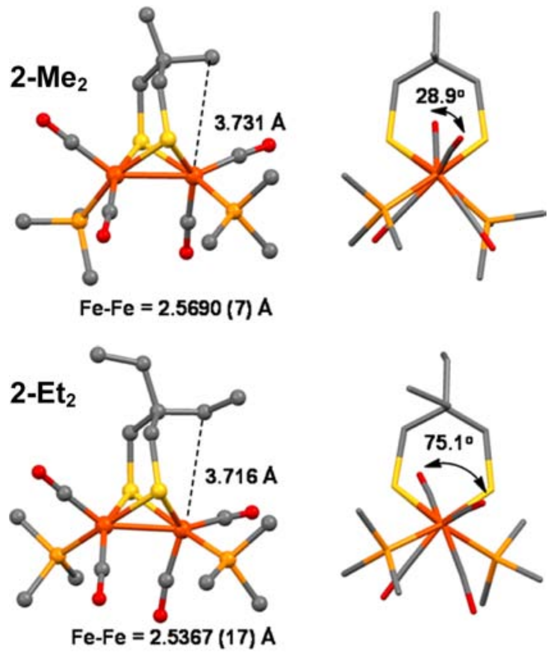

Figure 3. Structures of complexes **2-Me$_2$**[20] and **2-Et$_2$** with side view (left; ball-and-stick renditions) and end view (right; capped-stick renditions). Hydrogen atoms have been omitted for clarity. Full metric data of complexes **2-Me$_2$** and **2-Et$_2$** are listed in the Supporting Information (Table S1). Distances indicated are from the C-α to the central bridgehead carbon and the Fe center.

Scheme 1 presents the result of addition of two oxidants, the outer-sphere oxidant, ferrocenium, and nitrosonium, a possible inner sphere and noninnocent oxidant, to **2-Me$_2$** and **2-Et$_2$**, respectively, as monitored by IR spectroscopy. In both cases, a single cationic product is obtained with ν(CO) IR spectra that show two intense bands at higher wavenumbers, consistent with diminished π-backbonding, as compared to the neutral precursors. In both products a low intensity broad band appears in the 1850−1870 cm^{-1} region that indicates a bridging carbonyl. With the NO^+ oxidant an additional intense band at 1786 cm^{-1} is assigned to Fe-bound NO, indicating isoelectronic replacement of CO. Thus, these products, as BF_4^- salts, are designated as **2$_{NO}$-Me$_2$** or **2$_{NO}$-Et$_2$**; the products from reaction of the outer-sphere oxidant, Fc^+, are PF_6^- salts of **2$_{ox}$-Me$_2$** and **2$_{ox}$-Et$_2$**. Most importantly, the nitrosyl derivatives are diamagnetic, whereas the **2$_{ox}$-Me$_2$** and **2$_{ox}$-Et$_2$** species are S = 1/2, parramagnetic species. While both **2$_{ox}$-Me$_2$** and **2$_{ox}$ -Et$_2$** are thermally unstable, the greater stability of the latter permits EPR measurements at room temperature, vide infra.

Crystals of **2$_{NO}$-Me$_2$** and **2$_{NO}$-Et$_2$** (see the Supporting Information, Tables S2 and S3, for details of crystallization) were subjected to X-ray diffraction analysis, and their structures are shown in Figure 4. The PMe_3 ligands in both cations remain in transoid, basal positions, and the iron underneath the nearest Me or Et substituent on the bridgehead carbon has a largely open face, Fe_d. The view of the structures along the Fe−Fe vector shows carbonyls (apical within SP coordination environments on each iron) in transoid positions as one unit has twisted relative to the other. As compared to the parent complexes **2-Me$_2$** and **2-Et$_2$**, the distance between iron and the carbon α to the bridgehead, has decreased by ca. 0.3 Å. The flap angles (the angle between the mean planes comprising the three CH_2 units and that composed of the two CH_2S units) of complexes **2$_{NO}$-Me$_2$** and **2$_{NO}$-Et$_2$** are ca. 6° larger than that in the **2$_{NO}$** complex, (μ-pdt)[$Fe(CO)_2PMe_3$][$Fe(CO)(NO)$-PMe_3]$^+$,[30] which also indicates that relief of steric pressure at the bridgehead permits a H atom on the carbon α to the bridgehead C to rest in close proximity to the Fe_d.

Consistent with the well-defined μ-CO IR signal at 1875 cm^{-1} in the IR spectra of **2$_{NO}$-Me$_2$** and **2$_{NO}$-Et$_2$**, the $\angle_{Fe-C-O}$ of the bridging carbonyl in each is ca. 150°. No evidence of isomeric forms was found for **2$_{NO}$-Me$_2$** or **2$_{NO}$-Et$_2$** as was noted for the sterically unencumbered analogue, (μ-pdt)[Fe-$(CO)_2PMe_3$][$Fe(CO)(NO)PMe_3$]$^+$.[30]

Structures of the cations **2$_{ox}$-Me$_2$** and **2$_{ox}$-Et$_2$** are shown in Figure 5, rendered in ball and stick connectivities. Figure 6 highlights the structural similarities of **2$_{ox}$-Me$_2$** (blue)[20] and **2$_{NO}$-Me$_2$** (red); in each the PMe_3 ligands occupy transoid, basal positions. Note the distance between iron and carbon α to the bridgehead decreases by ca. 0.2 Å from **2$_{NO}$-Me$_2$** to **2$_{ox}$-Me$_2$**. The structural features deriving from the steric influence of the bridgehead carbon and the carbon atoms α to the bridgehead, noted in the metric parameters presented in Figures 4 and 5, will be further analyzed in the computational section of this manuscript presented below.

Solution Electrochemistry. Cyclic voltammograms of (μ-pdt)[$Fe(CO)_2PMe_3$]$_2$ (**2**), **2-Me$_2$** and **2-Et$_2$** in CH_2Cl_2 or

Scheme 1. Outer-sphere Oxidation (Fc$^+$) and Nitrosylation (NO$^+$/CO Exchange) of Complexes 2-Me$_2$ and 2-Et$_2$. IR Spectra for Complexes 2-Me$_2$, 2$_{NO}$-Me$_2$, 2$_{OX}$-Me$_2$ and 2-Et$_2$, 2$_{NO}$-Et$_2$, 2$_{OX}$-Et$_2$ in CH$_2$Cl$_2$

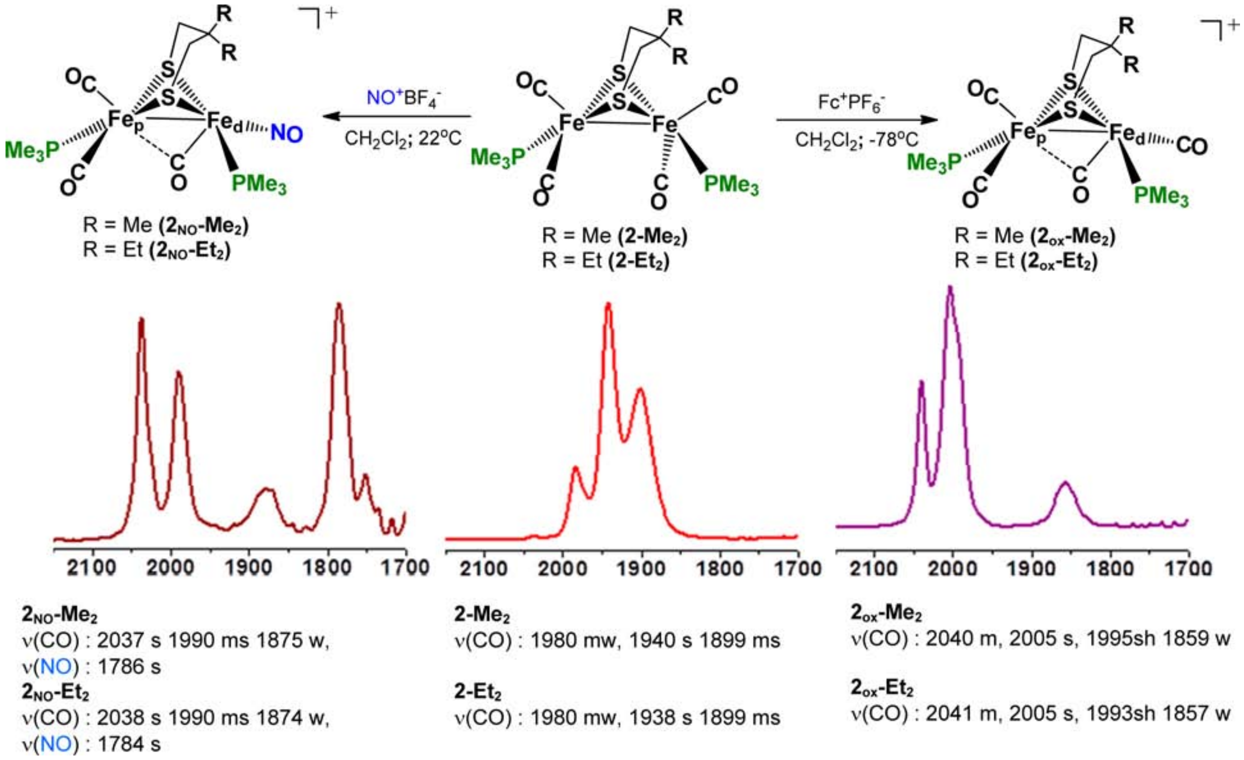

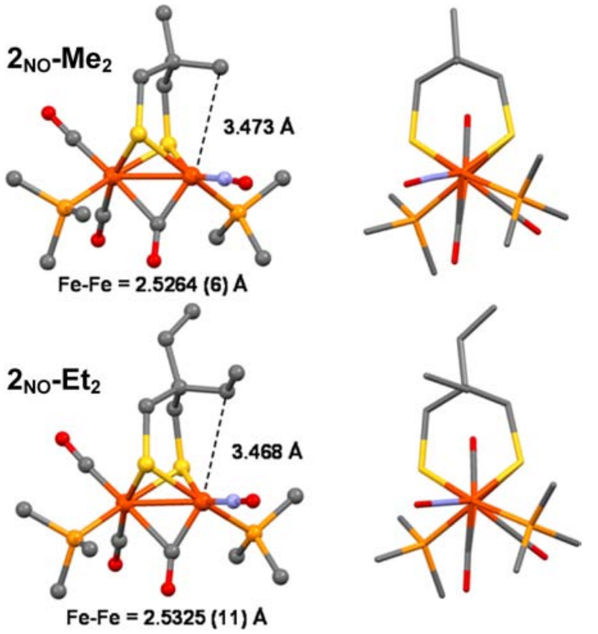

Figure 4. Molecular structures of complexes **2$_{NO}$-Me$_2$** and **2$_{NO}$-Et$_2$** with side view (left: ball-and-stick renditions) and end view (right: capped stick renditions). Hydrogen atoms, BF$_4^-$ counterion, and CH$_2$Cl$_2$ packing solvent have been omitted for clarity.

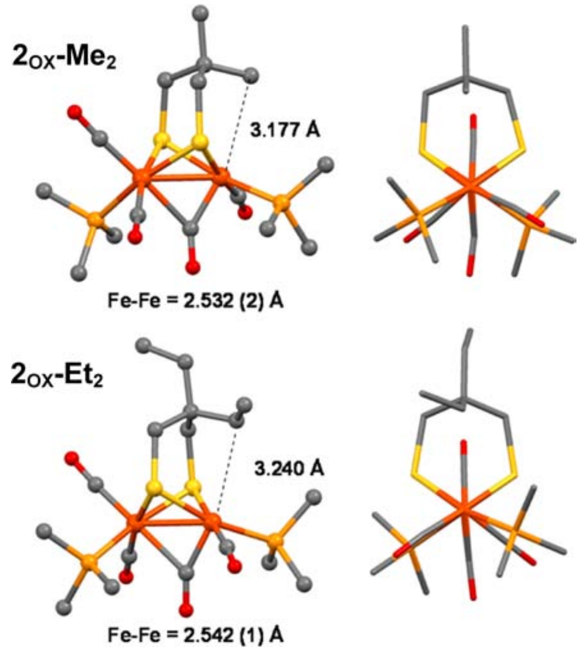

Figure 5. Molecular structures of complexes **2$_{ox}$-Me$_2$**[20] and **2$_{ox}$-Et$_2$** with side view (left: ball-and-stick renditions) and end view (right: capped stick renditions). Hydrogen atoms, PF$_6^-$ counterion, and CH$_2$Cl$_2$ packing solvent have been omitted for clarity.

CH$_3$CN solution find irreversible reductions at very negative potentials (ca. −2.1 V vs Fc/Fc$^+$), while a quasi-reversible oxidation for complex **2** (ca. E$_{1/2}$ = −0.15 V in CH$_3$CN) becomes fully reversible in **2-Me$_2$** and **2-Et$_2$**.[20] The oxidative event is assigned to Fe^{I}Fe^I/Fe^{II}Fe^I and is anodically shifted by ca. 200 mV (for **2-Me$_2$**)[20] and ca. 220 mV (for **2-Et$_2$**), as compared to complex **2** (Figure 7). According to the ν(CO) infrared values of **2**, **2-Me$_2$**, and **2-Et$_2$**, the propane, dimethylpropane, and diethylpropane dithiolates, pdt, dmpdt, and depdt, respectively, have similar electron-donating abilities and similar electronic effects on iron. Thus the electrochemical differences must be attributed to an influence of the steric effect

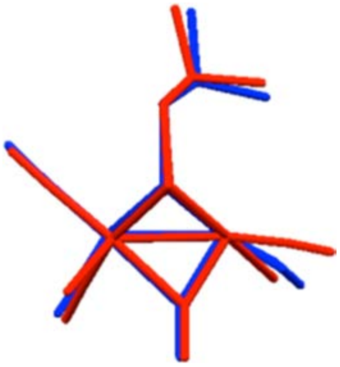

Figure 6. Overlay of the complex $\mathbf{2_{NO}}$-$\mathbf{Me_2}$ (red) with $\mathbf{2_{ox}}$-$\mathbf{Me_2}$ (blue) in capped-stick renditions. Hydrogen atoms, BF_4^- ($\mathbf{2_{NO}}$-$\mathbf{Me_2}$)/PF_6^-($\mathbf{2_{ox}}$-$\mathbf{Me_2}$) counterions and the methyl groups on the PMe_3 have been omitted for clarity.

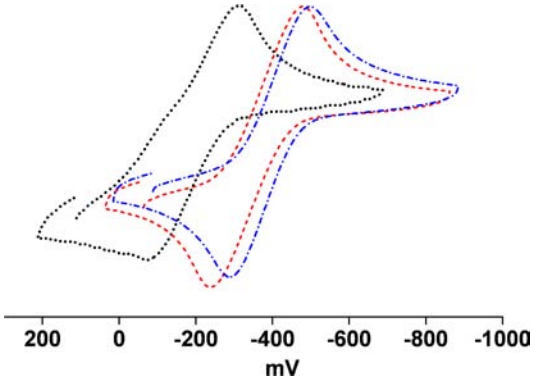

Figure 7. Cyclic voltammograms of complex **2** (black; dot line), **2-Me$_2$** (red; dash line), and **2-Et$_2$** (blue; dash-dot line) at scan rates of 200 mV in CH_3CN (vs Fc/Fc^+).

from the R groups on **2-Me$_2$** and **2-Et$_2$** that stabilizes the rotated, mixed-valent $Fe^{II}Fe^{I}$ state. Importantly, the reversibility of the oxidation waves suggested the possibility of isolating the mixed valent species according to the successful syntheses described above.[19,20]

As with complexes **2**, **2-Me$_2$**, and **2-Et$_2$**, the nitrosylated complexes $\mathbf{2_{NO}}$-$\mathbf{Me_2}$ and $\mathbf{2_{NO}}$-$\mathbf{Et_2}$ have terminal ν(CO) and ν(NO) stretching frequencies very similar to the nonsterically encumbered (μ-pdt)[Fe(CO)$_2$PMe$_3$][Fe(CO)(NO)PMe$_3$]$^+$, $\mathbf{2_{NO}}$.[30] Shown in Figure 8 are the cyclic voltammograms of complexes $\mathbf{2_{NO}}$-$\mathbf{Me_2}$ and $\mathbf{2_{NO}}$-$\mathbf{Et_2}$ which exhibits reversible and quasi-reversible couples centered at −1.11 and −1.47 V for $\mathbf{2_{NO}}$-$\mathbf{Me_2}$ and −1.11 and −1.48 V for $\mathbf{2_{NO}}$-$\mathbf{Et_2}$ (referenced to Fc/Fc^+) in CH_2Cl_2 (scan rate = 100 mV/s), respectively, with the remainder of the CV within the solvent window being blank (Figure 8, red dash line ($\mathbf{2_{NO}}$-$\mathbf{Me_2}$) and blue dash-dot line ($\mathbf{2_{NO}}$-$\mathbf{Et_2}$)). For complex $\mathbf{2_{NO}}$,[30] a less reversible CV pattern is displayed with reductive events centered at −1.09 and −1.47 V in CH_2Cl_2 (Figure 8, black dotted line). This difference in reversibility may be attributed to the presence of structural isomers in the nonsterically encumbered $\mathbf{2_{NO}}$. While specific oxidation states or redox levels have not been assigned, we have noted in exploratory studies of $\mathbf{2_{NO}}$-$\mathbf{Me_2}$ that only the more negative event shows a current increase with added aliquots of acetic acid. Studies to further probe the possibility and mechanism of the nitrosylated diiron complexes as hydrogen evolving catalysts are ongoing.

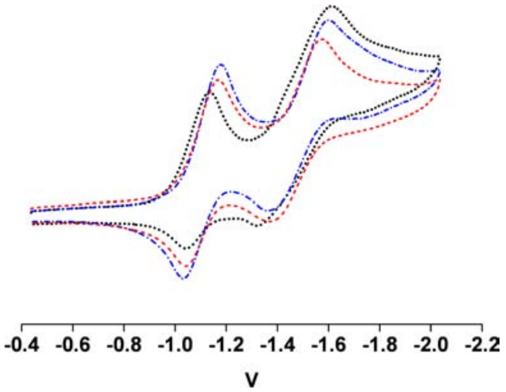

Figure 8. Cyclic voltammograms of complex $\mathbf{2_{NO}}$ (black; dot line), $\mathbf{2_{NO}}$-$\mathbf{Me_2}$ (red; dash line), and $\mathbf{2_{NO}}$-$\mathbf{Et_2}$ (blue; dash-dot line) at scan rates of 100 mV in CH_2Cl_2 (vs Fc/Fc^+).

Computational Investigations. *(μ-pdt)[Fe(CO)$_3$]$_2$, 1.* In order to compare parameters using the same computational metholodology on all compounds of interest, DFT calculations of complex **1** were revisited in its neutral $Fe^{I}Fe^{I}$, oxidized $Fe^{I}Fe^{II}$, and reduced $Fe^{0}Fe^{I}$ forms.[23] A simplistic analysis of the frontier molecular orbitals of **1**, Figure 9, suggests that the Fe−Fe bond order should be decreased on both removal of an electron from the HOMO, an orbital with Fe−Fe bonding character, and on addition of an electron to the LUMO, an orbital with Fe−Fe antibonding character. Figure 9 displays the frontier molecular orbitals (FMO's) of **1** as well as the optimized geometries, energies and SOMO's of the isomeric forms of the cationic $\mathbf{1_{ox}}$ and the anionic $\mathbf{1_{red}}$. The expansion of the Fe−Fe distance in both $\mathbf{1_{ox}}$ and $\mathbf{1_{red}}$ affirms the expectations of diminished bond order in these redox levels. The greater stability of the rotated structure in $\mathbf{1_{ox}}$ suggests that the stabilization of the semibridging carbonyl requires a short Fe−Fe distance that permits CO to be a donor to an electron-deficient Fe^{II}, in order to localize the electron deficiency in the mixed-valent, oxidized species. From Figure 9 it is clear that the

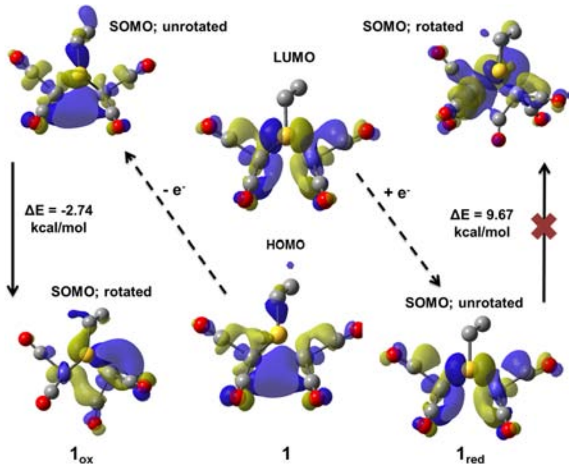

Figure 9. Frontier molecular orbitals of **1** and oxidized and reduced derivatives ($\mathbf{1_{ox}}$ and $\mathbf{1_{red}}$, respectively). The energy difference between the rotated and unrotated states, ΔE, for $\mathbf{1_{ox}}$ and $\mathbf{1_{red}}$ are given. Dashed arrows represent redox events originating from **1**, HOMO or LUMO, to unchanged geometries (unrotated) with subsequent possibilities of structural changes (rotated; solid arrows). Molecular orbitals were generated at an isosurface value of 0.030.

SOMO of $\mathbf{1_{ox}}$ is equally distributed between the irons in the unrotated (symmetrical) form; a shift of electron density toward the distal iron (open face) occurs on rotation. Note that the longer Fe to Fe distance in the electron-rich Fe^IFe^0 mixed-valent complex does not warrant a bridging CO; in fact the predicted Fe—S bond elongation suggests S-deligation at the bridge site better stabilizes the reduced form, vide infra.

The values presented in Figure 9 result from computations utilizing the B3LYP functional and the basis sets described in the Experimental Section. For this methodology the rotated structure is favored for $\mathbf{1_{ox}}$ by 2.74 kcal/mol over the unrotated structure, while for BP86 this difference is 4.04 kcal/mol. A previous study of **1** and $\mathbf{1_{ox}}$ with different basis sets gave a solution where the unrotated state is more stable than the rotated state, albeit by a mere 1.4 kcal/mol.[9b,15] Thus, it is clear that regardless of the method, the calculated energies of the rotated and unrotated $\mathbf{1_{ox}}$ complexes are close. In contrast, the Fe^0Fe^I state, $\mathbf{1_{red}}$, shows much larger energy differences in rotated vs unrotated states, 9.67 kcal/mol by B3LYP and 7.73 kcal/mol with BP86, permitting confidence in the conclusion stated above that a bridging carbonyl does not enhance stabilization of a rotated diiron arrangement for Fe^0Fe^I. It should be noted that the calculated structure of unrotated $\mathbf{1_{red}}$, finds one Fe—S bond to be broken, an effect that has been noted in earlier studies of other model complexes.[23,34]

Complexes with Bridgehead Steric Bulk: PMe_3 and Oxidized Derivatives. Geometric parameters calculated for **1-Me$_2$** and **1-Et$_2$**, the bis-phosphine derivatives, **2-Me$_2$** and **2-Et$_2$**, their one-electron oxidized states, $\mathbf{2_{ox}}$**-Me$_2$** and $\mathbf{2_{ox}}$**-Et$_2$**, and their NO^+ derivatives, $\mathbf{2_{NO}}$**-Me$_2$** and $\mathbf{2_{NO}}$**-Et$_2$**, match well with experimental results, Table 1. The calculated diatomic ligand stretching frequencies reasonably agree with experimental (solution) IR data, Table 2. The gas-phase calculated values for cationic complexes are systematically ca. 20 cm^{-1} larger than solution results. The B3LYP functional and the mixed basis sets (ECP for Fe and all-+electron for other atoms, see the Experimental Section) were used for the computations.

Table 1. Experimental and *Computational* Structure Details for Complexes 1 and 2

complexes	Fe—Fe (Å)	C_{ap}—Fe_p—Fe_d—L_{ap}[a]	C—Fe_d (R—Fe_d)[b] (Å)	flap angle[c]
1-Me$_2$	2.494	6.50	3.735 (3.753)	135.7
	2.509	*0.03*	*3.844 (3.941)*	*(138.8)*
1-Et$_2$	2.502	15.80	3.751 (3.775)	136.6
	2.507	*7.75*	*3.835 (3.869)*	*(137.1)*
2-Me$_2$	2.569	28.94	3.707 (3.731)	141.5
	2.567	*49.34*	*3.791 (3.827)*	*(137.2)*
2-Et$_2$	2.537	75.07	3.741 (3.716)	136.2
	2.562	*54.70*	*3.818 (3.817)*	*(137.1)*
$\mathbf{2_{NO}}$**-Me$_2$**	2.527	103.16	3.604 (3.473)	130.2
	2.584	*87.58*	*3.689 (3.621)*	*(133.8)*
$\mathbf{2_{NO}}$**-Et$_2$**	2.533	94.59	3.593 (3.468)	130.6
	2.582	*88.01*	*3.703 (3.626)*	*(134.0)*
$\mathbf{2_{ox}}$**-Me$_2$**	2.532		3.419 (3.177)	123.1
	2.594		*3.581 (3.393)*	*(129.5)*
$\mathbf{2_{ox}}$**-Et$_2$**	2.542		3.483 (3.240)	128.5
	2.592		*3.570 (3.324)*	*(128.8)*

[a] In $\mathbf{2_{NO}}$**-R$_2$** complexes (R = Me or Et), the second L_{ap} refers to the NO ligand. [b] Fe_d indicates the iron underneath the bridgehead. C—Fe_d refers to the distance of the central carbon of the S—CH_2—CR_2—CH_2—S (R = Me or Et) bridgehead, whereas R—Fe_d refers to the distance between the α-C of the R group of the central bridgehead carbon to the iron. [c] Angle between the mean planes comprised of the CH_2—CR_2—CH_2 units and that containing the two CH_2S units.

Table 2. Experimental and *Computational* IR Data of Complexes 1 and 2

complexes	vibrational frequencies[a] (cm^{-1})
1-Me$_2$	2075 m, 2034s, 2005s, 1992 ms, 1980mw[b]
	2074, 2022, 2005, 1994
1-Et$_2$	2073 m, 2031s, 2005s, 1990 ms, 1979mw[b]
	2073, 2021, 2004, 1993
2-Me$_2$	1980mw, 1940s, 1899 ms[c]
	1978, 1945, 1935, 1889
2-Et$_2$	1980mw, 1938s, 1899 ms[c]
	1978, 1942, 1935, 1885
$\mathbf{2_{NO}}$**-Me$_2$**	2037s, 1990 ms, 1875w, (1786s)[c]
	2057, 2027, 1899, (1813)
$\mathbf{2_{NO}}$**-Et$_2$**	2038s, 1990 ms, 1874w, (1784s)[c]
	2056, 2026, 1897, (1811)
$\mathbf{2_{ox}}$**-Me$_2$**	2040 m, 2005s, 1995sh, 1859w[c]
	2063, 2030, 2027, 1883
$\mathbf{2_{ox}}$**-Et$_2$**	2041 m, 2005s, 1993sh, 1857w[c]
	2061, 2029, 2027, 1877

[a] Vibrational frequencies have been scaled from their original calculated values by a factor of 0.9679. Values in bracket indicated nitrosyl stretching frequencies. [b] In hexanes. [c] In CH_2Cl_2.

Interesting to note is the torsion angle parameter L_{ap}—Fe—Fe—L_{ap}, in which the solid-state experimental/calculated match is within 8° for the all-carbonyl diiron complexes **1-Me$_2$** and **1-Et$_2$**. However, in disagreement with the solid-state experimental values of 28.94° (**2-Me$_2$**) and 75.07° (**2-Et$_2$**), the torsion angle values for **2-Me$_2$** and **2-Et$_2$** are calculated to be almost the same, around 50°. This indicates that, as calculated in the gas phase, the steric effect of the bridgehead is determined by the first carbon substituent, roughly equivalent for Me and Et upon interaction with the apical CO site. This computational result is consistent with solution electrochemistry as well as solid state vs solution ν(CO) IR spectra, vide supra. We conclude that intermolecular crystal packing effects account for differences in the degree of rotation of the apical carbonyl residing below the steric bulk of the bridgehead in the solid state of **2-Me$_2$** and **2-Et$_2$** complexes.

Due to equivalent steric effects of methyl and ethyl derivatized bridgeheads indicated in the gas-phase calculation, the following discussion focuses on **2-Me$_2$** and the cationic $\mathbf{2_{ox}}$**-Me$_2$** and $\mathbf{2_{NO}}$**-Me$_2$** derivatives; unless otherwise noted, all conclusions apply to the analogous **2-Et$_2$** complexes.

Computational Investigation of 2_{ox}-Me$_2$ and 2_{NO}-Me$_2$. The reaction of **2-Me$_2$** and **2-Et$_2$** with $Fc^+PF_6^-$ as outer-sphere oxidant, and with $NO^+BF_4^-$ as isoelectronic CO/NO^+ replacement, result in cationic diiron products of similar "rotated" structures; however, $\mathbf{2_{ox}}$**-Me$_2$** and $\mathbf{2_{ox}}$**-Et$_2$** exhibit paramagnetism while the $\mathbf{2_{NO}}$**-Me$_2$** and $\mathbf{2_{NO}}$**-Et$_2$** complexes are diamagnetic. The one-electron, outer-sphere oxidation results in complexes polarized to an apparent $Fe^{II}Fe^I$ state, as indicated by the SOMO (Figure 10) and unpaired spin density (Figure S6, Supporting Information) of $\mathbf{2_{ox}}$**-Me$_2$**. The (formal) oxidation states were assigned based on the percentage contribution to the SOMO, which suggests that the Fe_p contributes 10% (based on gross orbital population) whereas the contribution from the iron under the bridgehead, Fe_d, is 31%. The spin density plots of $\mathbf{2_{ox}}$**-Me$_2$** and $\mathbf{2_{ox}}$**-Et$_2$** confirm this

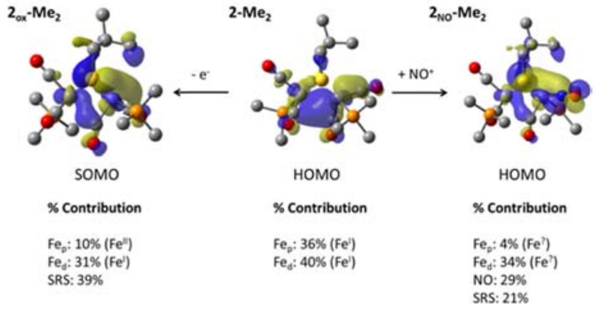

Figure 10. Highest occupied orbitals of **2_{ox}-Me$_2$**, **2-Me$_2$**, and **2_{NO}-Me$_2$**, from left to right. In all cases, emphasizing the connection to the [FeFe]-H_2ase active site structure, the Fe$_p$ indicates the iron at left in each diiron image and Fe$_d$ to the right and under the bridgehead; the latter is the "rotated SP iron" in **2_{ox}-Me$_2$** and **2_{NO}-Me$_2$**. Molecular orbitals were generated at an isosurface value of 0.030.

distribution, displaying the majority of the unpaired spin density on the Fe$_d$, with smaller contribution from the other iron. These results will be further tested by the high field Mössbauer and HYSCORE investigations of these compounds that are underway. The computational results described above are consistent with original spin density analyses of **2_{ox}-Me$_2$**[20] and are consistent with a spin density analysis of an oxidized NHC Fe—Fe derivative, which indicated the majority of the unpaired spin density to be on Fe$_d$, the rotated iron.[20,35]

Despite the difference in magnetism, the electronic distribution in **2_{NO}-Me$_2$**, is similar to that of **2_{ox}-Me$_2$**. The effect of NO$^+$ substitution for CO substantially polarizes the Fe—Fe bond to the extent of producing almost identical electronic character distribution for the SOMO of **2_{ox}-Me$_2$** and the HOMO of **2_{NO}-Me$_2$**. The conclusion to be drawn from the experimentally determined structures, as supported by computations, is as follows: *the NO$^+$ has effectively shifted electron density from the Fe^{I}Fe^I bond, repositioning it onto the Fe—N—O unit such that steric repulsion is sufficient to induce the rotated structure*. Overall the electronic distribution in **2_{NO}-Me$_2$**, is such that the Fe$_p$ has an oxidation state close to Fe^{II}, with the Fe$_d$ engaged in a Enemark/Feltham $\{Fe^I(^\bullet NO)\}^8$ unit.[36]

An extensive computational literature, primarily developed by the groups of Ghosh and Neese, explores the electronic effects of delocalized iron nitrosyl complexes.[37−41] Hopmann et al. addressed a series of iron nitrosyl complexes with various ligand environments, number of metal centers, and number of nitrosyl ligands attached to a given metal.[38] In such cases, it was concluded that the electronic states were generally high spin iron centers bound to $S = 1$, anionic nitroxide ligands. In contrast, the Fe—Fe—NO complexes reported herein are presumed to have low spin iron centers owing to the organometallic ligand environment.[38] Supporting our assumption is the statement by Ghosh and co-workers that low spin populations are consistent with strong antiferromagnetic coupling between metal and NO units, which is reflected in the molecular orbital analysis (see Figure 9) and spin population analysis (Table S6, Supporting Information).[38] The nature of the HOMO of **2_{NO}-Me$_2$** indicates electronic density on the "Fe$_d$" atom is in a bonding configuration to the NO nitrogen, which is in turn antibonding with respect to its oxygen. Such an arrangement accommodates the spin coupling that accounts for the observed diamagnetism of **2_{NO}-Me$_2$** and **2_{NO}-Et$_2$**.

Note two important factors in both the HOMO and SOMO of **2_{NO}-Me$_2$** and **2_{ox}-Me$_2$**: (1) the Fe centers are nonequivalent, with more electron density on Fe$_d$ relative to Fe$_p$; and (**2**) some electronic character appears delocalized onto the carbon substituent in the S—CH$_2$—CR$_2$—CH$_2$—S bridgehead. As the nearest hydrogen atom on the R groups to the Fe^I atom falls to within 3.2 Å in both the oxidized and nitrosylated complexes (as compared to 3.7 Å in the Fe^{I}Fe^I complexes), it is tempting to invoke a through-space interaction to the open site on the Fe^I.

EPR Investigations. *CW EPR Spectroscopy of the Complex **2_{ox}-Et$_2$**.* Earlier computations on complex **A** (Figure 2) found that unpaired spin density was located on the open site of the rotated iron (NHC-bound Fe).[35] This result was consistent with the weak and unresolved ^{31}P super hyperfine coupling (SHFC) in the continuous wave EPR spectrum of **A**.[18] In contrast, complex **C** (**2_{ox}-Me$_2$**) displays a strong ^{31}P SHFC, accounted for by the presence of the phosphine within the Fe^I (d^7) coordination sphere, which was also supported by DFT calculations.[20] An additional weak interaction led to line broadening, possibly a result of the phosphine on the adjacent iron, which in our interpretation is the oxidized low spin Fe^{II} (d^6).

Previously reported rotated mixed-valent models, complexes **A** and **2_{ox}-Me$_2$**, are not stable at room temperature. Presumably due to enhanced stability resulting from the bulky ethyl group on the bridgehead, EPR measurements of complex **2_{ox}-Et$_2$** could be acquired at both 10 and 295 K, and these are presented in parts a and b, respectively, of Figure 11. The EPR spectrum of **2_{ox}-Et$_2$** as its PF$_6^-$ salt in frozen CH$_2$Cl$_2$/THF solution displays a rhombic signal, which is similar to that of **2_{ox}-Me$_2$**[20] at 10 K with $g_1 = 2.010$, $g_2 = 2.031$, $g_3 = 2.086$. The room temperature, liquid phase EPR measurement of complex **2_{ox}-Et$_2$** (Figure 11b) exhibits a well-resolved isotropic spectrum with a doublet hyperfine splitting at $g_{av} = 2.044$ and ^{31}P SHFC ($A_{iso} = 74.62$ MHz). Thus, only one of the PMe$_3$ ligands is detected, indicating localization of an unpaired electron at the Fe^I in the 2Fe2S cluster.

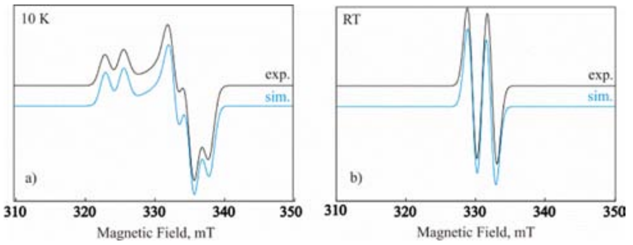

Figure 11. X-band CW EPR spectra of complex **2_{ox}-Et$_2$** (a) at 10 K and (b) at room temperature: experimental, black spectra; simulation, blue spectra. Simulation parameters for (a) g $(x, y, z) = (2.014, 2.031, 2.086)$; g-strain $(x, y, z) = (0.0096, 0.0087, 0.0104)$; ^{31}P SHFC A $(x, y, z) = -77.55, -70.05, -76.26)$ MHz. Simulation parameters for (b) $g_{av} = 2.044$; ^{31}P SHFC $A_{iso} = 74.62$ MHz.

*Pulsed EPR Spectroscopy of the Complexes **2_{ox}-Me$_2$** and **2_{ox}-Et$_2$**.* In order to obtain more detailed information about the spin density distribution in the iron complex, advanced pulsed EPR techniques were carried out for the mixed valence complexes **2_{ox}-Me$_2$** and **2_{ox}-Et$_2$**. The respective Q-Band FID-detected EPR spectra are presented in Figure 12. The simulation of the first derivative of both spectra is performed assuming a single $S = 1/2$ paramagnetic species with only one

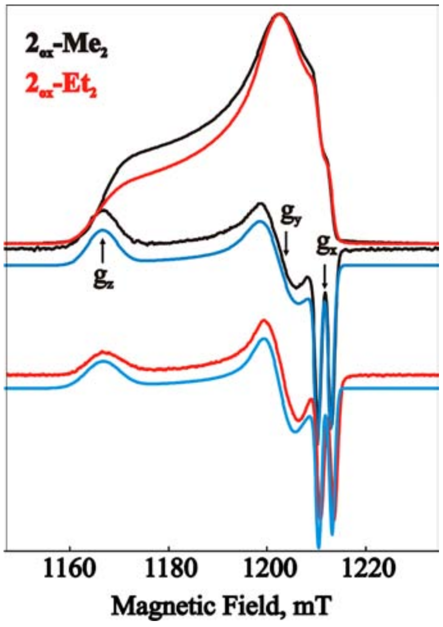

Figure 12. Q-band FID detected EPR spectra of **2_{ox}-Me$_2$** (black), **2_{ox}-Et$_2$** (red), pseudomodulated spectra of **2_{ox}-Me$_2$** (black), **2_{ox}-Et$_2$** (red), and corresponding simulations (blue). Simulation details are given in Tables 3 and 4.

Table 3. Experimental and *DFT-Calculated* *g*-Values for Complexes 2_{ox}-Me$_2$ and 2_{ox}-Et$_2$

complex	*g*-value (*x*, *y*, *z*) from EPR	*g-value* (*x*, *y*, *z*) from DFT
2_{ox}-Me$_2$	(2.013, 2.031, 2.086)	*(2.015, 2.038, 2.081)*
2_{ox}-Et$_2$	(2.014, 2.031, 2.086)	*(2.014, 2.037, 2.079)*

^{31}P SHFC. The simulation details are given in Table 3. The relatively strong ^{31}P SHFC for both complexes suggests a localization of spin density on one of the irons, i.e., $(A_{iso})_1$ (^{31}P) = −75.03 MHz and −74.62 MHz for **2_{ox}-Me$_2$** and **2_{ox}-Et$_2$**, respectively.

According to DFT analysis of the two complexes (see Figure 10), the iron with the "rotated" coordination geometry carries most of the spin density. The "unrotated" iron center, however, seems to also carry residual spin density. To verify how this weak spin density is reflected in the ^{31}P SHFC of the coordinating PMe$_3$ ligand, pulsed ^{31}P ENDOR experiments were carried out. The orientation selective Q−Band Davies ENDOR spectra for complexes **2_{ox}-Me$_2$** and **2_{ox}-Et$_2$** are presented in Figures 13 and 14. The low frequency ENDOR signals (between 14 and 28 MHz) can be assigned to the weakly coupled ^{31}P nucleus of the PMe$_3$ ligand of the "unrotated iron", Fe$_p$. The peak positions vary only slightly when the observing field is changed from the g_x to g_y and g_z positions. This indicates a relatively isotropic ^{31}P hyperfine interaction (see Table 4). The ENDOR peaks associated with the hyperfine interaction of the strongly coupled ^{31}P nucleus can also be observed (around 20 and 58 MHz) at g_x. The positions of these signals are consistent with the hyperfine interaction already observed in the CW spectrum (see Figures 11 and 12). The simulation parameters for both principal ^{31}P SHF coupling tensor components are given in Tables 3 and 4.

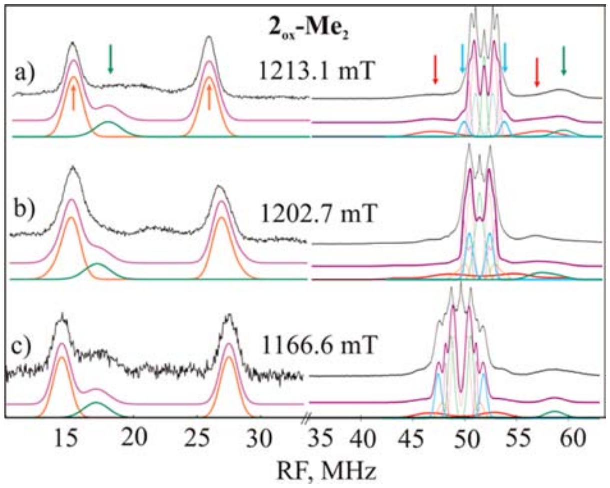

Figure 13. Q-band Davies ENDOR spectra of **2_{ox}-Me$_2$** (black) recorded at (a) 1213.1 mT (near g_x), (b) 1202.7 mT (near g_y), and (c) 1166.6 mT (near g_z), at 15 K, and corresponding total simulation (purple) assuming one ^{31}P$_{weak}$ SHFC (orange), one ^{31}P$_{strong}$ SHFC (green), one strong ^{1}H SHFC (red), one intermediate SHFC (blue), and four weak SHF couplings. Simulation parameters are collected in Table 4.

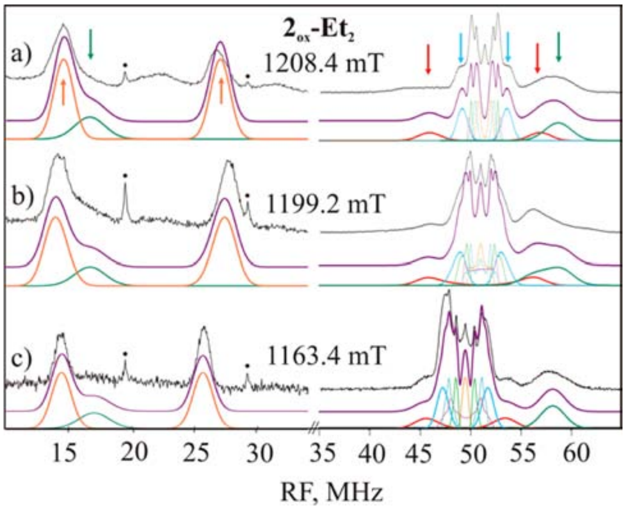

Figure 14. Q-band Davies ENDOR spectra of **2_{ox}-Et$_2$** (black) recorded at (a) 1208.4 mT (near g_x), (b) 1199.2 mT (near g_y), and (c) 1163.4 mT (near g_z), at 15K, and the corresponding total simulation (purple) assuming one ^{31}P$_{weak}$ SHFC (orange), one ^{31}P$_{strong}$ SHFC (green), one strong ^{1}H SHFC (red), one intermediate SHFC (blue), and four weak SHF couplings. Simulation parameters are collected in Table 4. * indicates instrumental artifacts.

The weak ^{31}P SFHC of −11.89 and −13.02 MHz for **2_{ox}-Me$_2$** and **2_{ox}-Et$_2$**, respectively, suggests a small delocalization of the spin density toward the "unrotated" iron, Fe$_p$, according to our interpretation, Fe^{II}. The predicted magnetic interaction parameters are presented in Tables 3 and 4. The DFT calculated SHFC values for both ^{31}P$_{weak}$ and ^{31}P$_{strong}$ are consistent with the experimental values and show the same trend (Figures 13, 14 and Table 4); i.e., the diethyl derivative as compared to the dimethyl complex shows a slight increase in the ^{31}P$_{weak}$-SHFC while the ^{31}P$_{strong}$-SHFC slightly decreases.

The ENDOR spectra of complex **2_{ox}-Me$_2$** and **2_{ox}-Et$_2$** presented in Figures 13 and 14, respectively, also show several well-resolved ^{1}H couplings. The ^{1}H hyperfine pattern could be

Table 4. Experimental and *DFT-Calculated* ^{31}P and ^{1}H SHFC Parameters of Complexes $\mathbf{2_{ox}\text{-}Me_2}$ and $\mathbf{2_{ox}\text{-}Et_2}$

					Euler angles (deg)		
nucleus	A_x (MHz) exptl DFT	A_y (MHz) exptl DFT	A_z (MHz) exptl DFT	A_{iso} (MHz) exptl DFT	α exptl DFT	β exptl DFT	γ exptl DFT
$\mathbf{2_{ox}\text{-}Me_2}$							
$^{31}P_1$ (PMe_3)	−76.91	−70.88	−77.31	−75.03	0	30	−10
P(6)	*−84.91*	*−85.88*	*−109.31*	*−93.37*	*−16.6*	*60.5*	*−54.9*
$^{31}P_2$ (PMe_3)	−8.82	−11.67	−15.17	−11.89	15	20	45
P(5)	*−13.62*	*−17.27*	*−13.17*	*−14.69*	*14.3*	*23.9*	*44.5*
^{1}H $(Me_3)_{br}$	17.02	−8.88	−9.31	−0.37	25	25	−10
H(33)[a]	*18.35*	*−7.88*	*−6.32*	*−1.38*	*28.9*	*20.4*	*−7.9*
^{1}H (P_1Me_3)	1.34	2.21	4.48	2.68	−10	10	40
H(24)[a]	*1.68*	*1.78*	*4.68*	*2.71*	*−25.4*	*29.9*	*9.6*
$\mathbf{2_{ox}\text{-}Et_2}$							
$^{31}P_1$ (PMe_3)	−77.55	−70.05	−76.26	−74.62	−10	0	−20
P(5)	*−83.92*	*−108.09*	*−84.80*	*−92.27*	*−30.0*	*75.6*	*−26.3*
$^{31}P_2$ (PMe_3)	−13.02	−15.54	−10.51	−13.02	0	30	0
P(6)	*−13.85*	*−18.31*	*−14.33*	*−15.49*	*5.2*	*66.1*	*−60.7*
^{1}H (Ethyl)	−6.30	−5.01	13.22	0.64	10	30	0
H(31)[a]	*−8.35*	*−9.69*	*21.99*	*1.32*	*30.6*	*71.2*	*−22.3*
^{1}H (P_1Me_3)	6.69	3.69	2.49	4.29	−10	45	60
H(40)[a]	*1.15*	*4.07*	*1.25*	*2.16*	*−26.0*	*68.7*	*−29.2*

[a] Selected DFT-calculated ^{1}H SHFC are presented. The complete calculation can be found along with the numbers that identify specific atoms in Figures S7 and S8 in the Supporting Information. [b] SHFC signs are determined by DFT calculations.

simulated using a minimum of six proton couplings (Table 4). Only two of these couplings could be tentatively assigned: As can been seen from Figures 13 and 14, the strongest ^{1}H SHFC (around 10 MHz) is present in both complexes. This signal can be simulated by assuming a quite dipolar ^{1}H SHFC (Table 4). For $\mathbf{2_{ox}\text{-}Et_2}$, the strongest DFT-calculated ^{1}H SHFC (−8.35, −9.69, 21.99) MHz originates from one of the depdt protons pointing "downwards" into the open coordination site. The corresponding carbon atom has a distance of 3.240 Å to the "rotated" iron (see Figure 5, $\mathbf{2_{o}x\text{-}Et_2}$). The DFT-calculated SHFC for this proton fits the observed strongest ^{1}H coupling remarkably well. It is therefore tempting to assign this strongly coupled ^{1}H SHFC to the "downward pointing" ethyl proton (proton H(31) in Figure S8 in the Supporting Information). For $\mathbf{2_{ox}\text{-}Me_2}$, a similar assignment can be made for the methyl proton of the carbon atom at a distance of 3.177 Å to the "rotated iron" (see Figure 5). The calculated SHFC of this proton (18.35, −7.88, −6.32) MHz also fits the observed ^{1}H ENDOR splitting very well. It should, however, be noted that, in general, one would expect the methyl proton SHFC to be averaged due to fast rotation. The averaged methyl proton coupling for this group: (−3.34, −3.14, 7.72) MHz, however, does not fit the experimentally observed splitting. One could speculate that the rotation of the methyl group interacting with the open coordination site is hindered due to an agostic interaction of the methyl protons with the "rotated iron". Hindered rotation of methyl groups also has been observed in matrix isolated methyl radicals.[46]

A second characteristic ^{1}H SHFC is particularly well resolved for $\mathbf{2_{ox}\text{-}Et_2}$ at the field position corresponding to g_x. Signals consistent with this hyperfine tensor (1.68, 1.78, 4.68) MHz, but with slightly different orientation with respect to the g-tensor, are also observed for $\mathbf{2_{ox}\text{-}Me_2}$ (see Table 4). Owing to the more isotropic character (as compared to the outermost ^{1}H SFHC) and its relatively large spectral contribution, we attribute this signal to the methyl protons of the PMe_3 ligand. The difference in the field dependency of the ENDOR signal for the two complexes might be a result of a slight change in the orientation of the PMe_3 ligand (Figure 5). This change is also reflected in the ^{31}P ENDOR spectra of $\mathbf{2_{ox}\text{-}Me_2}$ vs the $\mathbf{2_{ox}\text{-}Et_2}$ complexes (Figures 13 and 14).

Mössbauer Spectroscopic Studies. Mössbauer spectroscopic studies have been used to probe the changes at the Fe sites in the series of well-characterized complexes $\mathbf{2\text{-}Me_2}$, $\mathbf{2_{ox}\text{-}Me_2}$, ($\mu$-H)($\mu$-dmpdt)-$[(Fe^{II}(CO)_2PMe_3]_2[BF_4]$ ($\mathbf{2_H\text{-}Me_2}$),[47] and $\mathbf{2_{NO}\text{-}Me_2}$, and to further evaluate them as models of the active site of the [FeFe]-hydrogenase.[48−50] Because each of these organometallic compounds revealed its own complexity, i.e., they eluded a simple correlation of formal oxidation state assignment (according to classic organometallic chemistry rules) with the expected increase in isomer shift, the Mössbauer results must be put in the context of a larger set of compounds.[31] For low-spin ferrous, ferric, and Fe^{I} complexes (inasmuch as low-spin Fe^{I} complexes have been studied), the isomer shift is relatively insensitive to changes in oxidation states and ligands, but small changes can be observed.[51,52] Moreover, given the noninnocent character of the NO ligand, it is hard to affirm decisive correlations between structural changes and isomer shifts.

The spectrum at 7 K of $\mathbf{2\text{-}Me_2}$ was fit with two Lorentzian lines (fwhm of 0.28 mm/s) with equal intensities, with parameters $\delta_{1,2}$ = 0.06, 0.07 mm/s and $\Delta E_{Q1,2}$= 1.00, 0.75 mm/s (Figure 15 and Table 5). Alternatively the spectrum could be fit with a Voight-shaped line (fwhm of −0.35 mm/s) with $\delta_1 = \delta_2$ = 0.06 and ΔE_Q = 0.85 mm/s. Such fits are not unique, but the parameters shown in Table 5 and Figure 15 gave the best least-squares fit. The isomer shift values are similar to the reduced state ($\delta \sim 0.08$ mm/s and $\Delta E_Q \sim 0.87$ mm/s) of the 2Fe subcluster in [FeFe]-hydrogenase.[48−50] The mixed-valence, $S = 1/2$, $Fe^{II}Fe^{I}$ complex $\mathbf{2_{ox}\text{-}Me_2}$ exhibits two sites, with equal contributions to the spectrum, having a distinctly higher isomer shift for one site (δ = 0.19, 0.09 mm/s and ΔE_Q = 1.04, 0.54 mm/s). These parameters are in the same range with those observed for the oxidized H_{ox} state ($0.1 < \delta <$

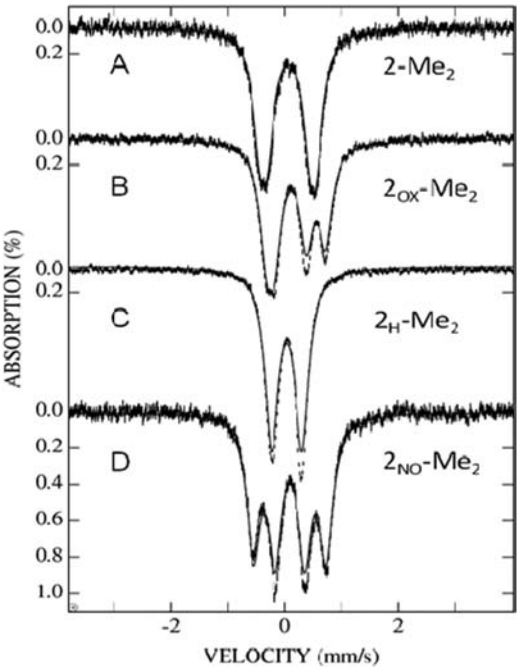

Figure 15. Mössbauer spectra (7 K, 0.4 mT) of complexes (A) **2-Me$_2$** (B) **2$_{ox}$-Me$_2$** (C) **2$_H$-Me$_2$**, and (D) **2$_{NO}$-Me$_2$**. The solid lines through the data are spectral simulations with the parameters in Table 5.

Table 5. Mössbauer Parameters of [FeFe]-hydrogenase and Model Complexes 2-Me$_2$, 2$_{ox}$-Me$_2$, 2$_{NO}$-Me$_2$, and 2$_H$-Me$_2$ (Isomer Shifts Are Quoted at 7 K with Respect to Fe Metal Standard at rt)

	isomer shift δ (mm/s)	quadrupole splitting ΔE_Q (mm/s)
reduced, **Fe^{I}Fe^I**, **H$_{red}$**[a]	~0.08	~0.87
oxidized, **Fe^{II}Fe^I**, **H$_{ox}$**[a]	$0.1 < \delta < 0.3$	$0.7 < \Delta E_Q < 1.2$
H$_{ox}$-CO[a]	0.17, 0.13	0.70, 0.65
2-Me$_2$, Fe^{I}Fe^I	0.06, 0.07	1.00, 0.75[b]
2$_{ox}$-Me$_2$, Fe^{II}Fe^I	0.19, 0.09	1.04, 0.54
2$_{NO}$-Me$_2$, Fe$^?$Fe$^?$	0.09	1.28, 0.52
2$_H$-Me$_2$, Fe^{II}Fe^{II}	0.04	0.50, 0.56

[a] Parameters of hydrogenase 2Fe-subcluster.[48−50] [b] Line widths are specified in the text. Uncertainties are 0.02 mm/s.

0.3 mm/s and $0.7 < \Delta E_Q < 1.2$ mm/s) of the 2Fe-subcluster.[49,50]

The large shifts in ν(CO) values (>50 cm^{-1}, see Supporting Information) on protonation of **2-Me$_2$** to **2$_H$-Me$_2$** are consistent with oxidative addition of H$^+$, producing a hydride ligand, ultimately residing in the bridging position between two formal Fe^{II} centers.[47,53] However the isomer shift value for each iron, $\delta = 0.04$, is actually *decreased* relative to the Fe^{I}Fe^I, and hence, according to usual interpretation, does not necessarily indicate full oxidation of the Fe^I centers. The complexities and nuances of redox level assignments that rely on spectroscopies that reflect different effects (ν(CO) IR reports primarily on changes in d-orbital electrons from π-backbonding while Mössbauer reports on s-density at iron) are addressed in the separate report.[31]

Complex **2$_{NO}$-Me$_2$** exhibits isomer shifts of 0.09 ± 0.02 mm/s and ΔE_Q = 1.28, 0.52 ± 0.02 mm/s which are qualitatively indicative of oxidation of both Fe^I centers in **2-Me$_2$**. As the EPR and magnetic susceptibility studies indicate that this compound is diamagnetic, and in agreement with the DFT results above, we conclude that the NO radical is coupled with the closest Fe^I, the Fe$_d$, while the adjacent iron, the Fe$_p$, has had substantial electron density shifted away from it. Thus we propose that the metal oxidation states of complex **2$_{NO}$-Me$_2$** are Fe^{II}Fe^I with the latter spin-coupled to an NO radical. Sufficient electronic density from the Fe^{I}Fe^I core, and the Fe−Fe bond, is removed by single electron, outer sphere (Fc$^+$) or noninnocent (NO$^+$) oxidants to make both **2$_{ox}$-Me$_2$** and **2$_{NO}$-Me$_2$** favor the rotated, bridging carbonyl structure, also consistent with the computational results.

SUMMARY AND COMMENTS

From biosynthetic/structural studies of the maturation processes of [FeFe]-H$_2$ase, Peters and Broderick have hypothesized that delivery and insertion of the diiron unit, premade on a scaffold protein, into the prepared cavity of the apo-hydrogenase protein are followed by a collapse of the surrounding peptide chain.[54] This collapse produces a snug cavity with outer sphere steric constraints on the unique "rotated" organodiiron unit that have been approximated in our study by positioning methyl or ethyl groups at the bridgehead of the S-to-S linker in the [FeFe]-H$_2$ase active site models. In fact, the fused FeS$_2$C$_2$X cyclohexane-like units that exist in boat and chair configurations are themselves sterically controlling units, even with hydrogen atoms at the bridgehead of the FeS$_2$C$_3$ hydrocarbon model. The steric effects of the chair-boat configurations are amplified via the dimethyl- and diethylpropane dithiolate units, especially in complexes wherein PMe$_3$ ligands have replaced CO ligands.

While the hundreds of (μ-pdt)Fe^{I}Fe^I complexes prepared as models of the [FeFe]-H$_2$ase active site find stability in the metal−metal bond of symmetrical, dithiolate−sulfur edge-bridged square pyramids, distortion is seen in the Fe^{I}Fe^I complexes with bridgehead bulk that are precursors of the stable oxidized Fe^{II}Fe^I complexes that have been isolated in our studies.[20] Either in full mixed-valent Fe^{II}Fe^I form produced from outer-sphere one electron oxidation, or in the ersatz mixed-valent form created by NO$^+$ substitution of CO (leading to shifts in electron distribution that Mössbauer and computational data implies to be at a redox level of Fe^{II}-{Fe^I($^\bullet$NO)}^{8}), structural rearrangement occurs producing the square pyramid/inverted square pyramid that matches that found in the active site structure of the H$_{ox}$ state of [FeFe]-H$_2$ase. In both of the oxidized models, the Fe−Fe distance is maintained with assistance from the bridging CO interaction and the relief of steric strain as the bridgehead methyl or ethyl groups in the boat form of the FeS$_2$C$_3$ cyclohexane-like units relax into the available space of the open site on the synthetic "distal iron". Thus, the combination of electronic effects that diminishes Fe−Fe bond order and steric effects that promote the structural rearrangement that accommodates the electron density shift are resolved in this organodiiron molecular construct.

The Mössbauer parameters and computational investigations suggest that in the Fe^{I}Fe^I state, the electronic densities of the Fe centers are essentially equivalent, with nearly identical isomer shift values, in agreement with the percentage contribution from the irons to the HOMO of **2-Me$_2$** or **2-Et$_2$** as well as the population analysis (Table S6, Supporting Information). A spin density analysis of the one-electron oxidized complex **2$_{ox}$-Me$_2$** or **2$_{ox}$-Et$_2$** demonstrates a localized Fe^{II}Fe^I complex, experimentally corroborated by the different isomer shift values of 0.19 and 0.09 mm/s, the latter of which is similar to the neutral complexes and thus represents the Fe^{I} metal center, Fe_d. The EPR and ENDOR results are in agreement with those from Mössbauer concluding that the $S = 1/2$ paramagnetism comes from largely localized $Fe^{II}Fe^{I}$ mixed valent species, with strong hyperfine coupling to one phosphine ligand, and weak coupling to the phosphine of the adjacent iron. More detailed ENDOR studies see further interactions with hydrogen atoms, apparently on a bridgehead substituent, although the hydrogens of the phosphine methyl groups are also nearby. From Mössbauer, electrochemistry, and CO vibrational frequencies, with complementary gas phase DFT results, the redox level of the nitrosylated species is found to be remarkably similar to that of the **2_{ox}-R_2** compounds. Such concurrence of redox levels in the two compounds results from the drain of electron density from the Fe−Fe bond and onto the nitrosyl ligand effectively reducing the NO^+ to the neutral NO radical, which with spin coupling to Fe^{I} maintains diamagnetism in a “mixed valent” Fe^{II}-$\{Fe^{I}(^{\bullet}NO)\}^{8}$.

Previous work had indicated that the rotated state of a given $Fe^{I}Fe^{I}$ model complex could be made more accessible by adding stronger electron donor ligands, increasing the steric bulk (NHC,[18] dppv ligands[19]), especially at the bridgehead ($SCH_2CR_2CH_2S$), or by one-electron oxidation (Fc^+) of the complex.[18,20] The work reported herein utilizes all of these features to access the fully rotated $Fe(CO)_2L$ unit in the oxidized Fe^{II}−Fe^{I} complex or in the nitrosylated Fe^{II}−$\{Fe^{I}(^{\bullet}NO)\}^{8}$ complex. However, while oxidation has the greatest effect on the ease, or energy cost, of rotation, a salient goal has been a stable rotated structure in the $Fe^{I}Fe^{I}$ redox level. By adding the steric bulk at the central bridgehead carbon, the C_{ap}−Fe_p−Fe_d−C_{ap} torsion angle values of 28.94° and 75.07° in the solid-state structures for **2-Me$_2$** and **2-Et$_2$**, respectively, even in the absence of an oxidation state change of the metal, are encouraging that the fully rotated state with an available site for H^+ addition and terminal, stable hydride formation can eventually be obtained even in the $Fe^{I}Fe^{I}$ complexes.

■ EXPERIMENTAL SECTION

General Materials and Techniques. All reactions and operations were carried out on a double-manifold Schlenk vacuum line or within a glovebox under N_2 or Ar atmosphere. THF, CH_2Cl_2, pentane, and diethyl ether were freshly purified by an MBraun manual solvent purification system packed with Alcoa F200 activated alumina desiccant. The purified THF, CH_2Cl_2, pentane, and diethyl ether were stored with molecular sieves under N_2 before experiments. The known complexes (μ-dmpdt)$[Fe(CO)_2PMe_3]_2$ (dmpdt = 2,2-dimethyl-1,3-propanedithiolate) (**2-Me$_2$**) and (μ-depdt)$[Fe(CO)_3]_2$ (**1-Et$_2$**) (depdt = 2,2-diethyl-1,3-propanedithiolate) were synthesized by published procedures.[20,32] The following materials were of reagent grade and were used as purchased from Sigma-Aldrich: trimethylphosphine, nitrosyl tetrafluoroborate, ferrocenium hexafluorophosphate, tetrabutylammonium hexafluorophosphate, and dichloromethane-d_2.

Physical Measurements. Nuclear magnetic resonance spectra were measured in CD_2Cl_2 solutions on a Unity+ 300 MHz superconducting NMR instrument and were referenced to residual CH_2Cl_2 at 5.32 ppm for ^1H spectra. Solution infrared spectra were recorded on a Bruker Tensor 27 FTIR spectrometer in CaF_2 solution cells of 0.1 mm path length. Solid-state samples were recorded using the Pike MIRacle attachment from Pike Technologies for Attenuated Total Reflectance Infrared Spectra, ATR-FTIR. All electrochemical analyses were done using a Bioanalytical System (BAS) 100 electrochemical workstation with a glassy carbon working electrode and a platinum wire auxiliary electrode. Voltammograms were obtained using a standard three-electrode cell under an argon atmosphere at room temperature. Samples in CH_3CN or CH_2Cl_2 were measured at a concentration of 2 mM with $[n\text{-}Bu_4N]PF_6$ as the supporting electrolyte (100 mM), and potentials are reported relative to the Fc/Fc^+ couple as 0.00 V. Mass spectrometry (ESI-MS) was performed by the Laboratory for Biological Mass Spectrometry at Texas A&M University. Elemental analyses were performed by Atlantic Microlab, Inc., Norcross, GA.

EPR Measurements. FID detected EPR and ENDOR measurements were performed on a Bruker ELEXSYS E580 Q-band pulse EPR spectrometer equipped with a SuperQ-FT microwave bridge and a home-built EPR/ENDOR TE_{011} resonator.[55] Radio frequency (RF) pulses were generated by means of an Agilent E4420B radiofrequency generator and a high-power RF amplifier: AR 2500 L from Amplifier Research (2.5 kW). Measurement conditions for ^{31}P Davies ENDOR (π-RF-$\pi/2$-τ-π-echo): optimized RF pulses: 35 μs for the low frequency range (0−35 MHz) and 5 μs for the high frequency range (35−65 MHz); microwave (MW) pulses ($\pi/2$): 24 ns. Measurement temperature was 15 K. Simulation of the spectra is based on the spin Hamiltonian approach. CW and ENDOR spectra were simulated using the EasySpin package.[56]

EPR sample preparation: A solution of the diiron complex (0.100 mmol) in 10 mL of THF/dichloromethane and cooled to −78 °C was added to a precooled tube containing solid ferrocenium hexafluorophosphate. (0.100 mmol). Diiron complex, oxidant, and the solvent were added into Schlenk tubes inside a drybox. Afterward, a Schlenk line was used while mixing. The reaction was allowed to stir for 30 min at low temperature. Finally, the precooled EPR tubes were filled under inert conditions.

Mössbauer Measurements. Low-field (300 G), variable-temperature (4.5−200 K) Mössbauer spectra were recorded on a closed-cycle refrigerator spectrometer, model CCR4K, equipped with a 0.038 T permanent magnet, maintaining temperatures between 4.5 and 300 K. Mössbauer spectra were analyzed using the software WMOSS (Thomas Kent, SeeCo.us, Edina, MN). The samples were polycrystalline powders, suspended in Nujol, placed in Delrin 1.00 mL cups, and frozen in liquid nitrogen. All manipulations before freezing were done in an oxygen-free glovebox.

X-ray Crystal Structure Analyses. A Bausch and Lomb 10× microscope was used to identify suitable crystals of the same habit. Each crystal was coated in paratone, affixed to a Nylon loop and placed under streaming nitrogen (110K) in a SMART Apex CCD diffractometer (see details in the .cif file). The space groups were determined on the basis of systematic absences and intensity statistics. The structures were solved by direct methods and refined by full-matrix least-squares on F^2. Anisotropic displacement parameters were determined for all nonhydrogen atoms. Hydrogen atoms were placed at idealized positions and refined with fixed isotropic displacement parameters. The following is a list of programs used: data collection and cell refinement APEX2;[57] data reductions, SAINTPLUS Version 6.63;[58] absorption correction, SADABS;[59] structural solutions, SHELXS-97;[60] structural refinement, SHELXL-97;[61] graphics and publication materials, Mercury Version 2.3.[62]

Synthesis of (μ-dmpdt)$[Fe(CO)_2PMe_3]$-$[Fe(CO)(NO)PMe_3]$-$[BF_4]$ (2_{NO}-Me$_2$). A solution of (μ-dmpdt)$[Fe(CO)_2PMe_3]_2$ (**1**) (0.102 g, 0.20 mmol) and $[NO][BF_4]$ (0.023 g. 0.20 mmol) in 15 mL of CH_2Cl_2 turned from red to dark brown after stirring for 30 min at 22 °C. Infrared spectroscopy confirmed reaction completion with no remaining starting material. The solution was filtered through celite to remove insoluble solid. After the reaction solution was concentrated to 5 mL, 30 mL of pentane was added to precipitate the product. The solid product was further washed with diethyl ether (3 × 10 mL). Yield: 0.099 g (83%). Layering of CH_2Cl_2 solution of **2_{NO}-Me$_2$** with a 2:1 mixture of pentane and diethyl ether afforded dark brown single crystals after 2 week at −35 °C. IR (cm^{-1}, in CH_2Cl_2): ν(CO) 2037 (s), 1991 (ms), 1877 (w); ν(NO) 1787 (s). ^1H NMR (CD_2Cl_2): 0.96 (m, 3H, CMe_2) 1.16 (s, CMe_2); 1.58 (d, 9H, PMe_3); 1.80 (d, 9H, PMe_3); 2.39 (m, 2H, SCH_2); 2.53 (d, 1H, SCH_2); 2.63 (d, 1H, SCH_2) ppm. ESI-MS+ (CH_2Cl_2): m/z = 511.98 ((μ-dmpdt)$[Fe(CO)_2PMe_3]$-

[Fe(CO)(NO)PMe$_3$]$^+$). Anal. Found (Calcd) for $C_{14}H_{28}BF_4Fe_2NO_4P_2S_2\cdot CH_2Cl_2$: C, 26.43 (26.34); H, 4.47 (4.42); N, 2.17 (2.05).

Reaction of 2_{NO}-Me$_2$ and CO. Carbon monoxide (^{12}CO) was bubbled into a 20 mL CH_2Cl_2 solution of complex **2_{NO}-Me$_2$** (0.060 g, 0.1 mmol) in a 100 mL Schlenk flask for 10 min. The flask was sealed at 1 atm CO atmosphere and stirred overnight at room temperature after which IR spectroscopy indicated that no μ-NO species was present.[30]

Synthesis of (μ-depdt)[(Fe(CO)$_2$PMe$_3$]$_2$ (2-Et$_2$). To a 200 mL Schlenk flask equipped with a reflux condenser and containing (μ-depdt)[(Fe(CO)$_3$]$_2$,[32] (0.45 g 1.0 mmol) was added 100 mL of dry toluene. The reaction was heated to 100 °C and PMe$_3$ (1 mL) was added. The reaction was monitored by IR and showed complete disappearance of the starting material after 48 h. Solvent was removed in vacuo and the resulting solid recrystallized with MeOH to give a dark red solid. Yield: 0.40 g (74%). Crystals of X-ray quality were obtained from a concentrated MeOH solution stored at −4 °C. IR (cm^{-1}, in CH_2Cl_2): ν(CO) 1980 (mw), 1938 (s), 1899 (ms). ^{1}H NMR (CD_2Cl_2): 0.70 (t, 6H, C(CH$_2$C*Me*$_2$)$_2$), 1.40 (q, 4H, C(C*H*$_2$CMe$_2$)$_2$) 1.48 (d, 18H, P*Me*$_3$), 2.03 (s, 4H, SC*H*$_2$) ppm. Anal. Found (Calcd) for $C_{17}H_{32}Fe_2O_4P_2S$: C, 37.91 (37.94); H, 6.17 (5.99); N, 0.00 (0.00).

Synthesis of (μ-depdt)[Fe(CO)$_2$PMe$_3$][Fe(CO)(NO)PMe$_3$][BF$_4$] (2_{NO}-Et$_2$). In a similar manner to that described for complex **2_{NO}-Me$_2$**, a mixture of (μ-depdt)[Fe(CO)$_2$PMe$_3$]$_2$ (**2-Et$_2$**) (0.11 g, 0.20 mmol) and [NO][BF$_4$] (0.023 g. 0.20 mmol) in 15 mL of CH_2Cl_2 resulted in a color change from red to dark brown after stirring for 30 min at 22 °C. The solution was filtered through celite to remove insoluble solid. After removal of solvent to 5 mL, the product precipitated upon addition of 30 mL of pentane. The solid product was further washed with diethyl ether (3 × 10 mL). Yield: 0.100 g (80%). Layering of a CH_2Cl_2 solution of **2_{NO}-Et$_2$** with a 2:1 mixture of pentane and diethyl ether afforded dark brown single crystals after three week at −35 °C. IR (cm^{-1}, in CH_2Cl_2): ν(CO) 2038 (s), 1990 (ms), 1874 (w); ν(NO) 1784 (s). ^{1}H NMR (CD_2Cl_2): 0.74 (t, 3H, C(CH$_2$C*Me*$_2$)$_2$), 0.86 (t, 3H, C(CH$_2$C*Me*$_2$)$_2$), 1.58 (q, 2H, C(C*H*$_2$CMe$_2$)$_2$), 1.58 (d, 9H, P*Me*$_3$), 1.80 (m, P*Me*$_3$ and C(C*H*$_2$CMe$_2$)$_2$), 2.30 (m, 2H, SC*H*$_2$), 2.59 (d, 2H, SC*H*$_2$), 2.69 (d, 2H, SC*H*$_2$) ppm. Anal. Found (Calcd) for $C_{16}H_{32}BF_4Fe_2NO_4P_2S_2\cdot CH_2Cl_2$: C, 28.33 (28.68); H, 4.52 (4.81); N, 2.08 (1.97). ESI-MS+ (CH_2Cl_2): m/z = 540.02 ((μ-depdt)[Fe(CO)$_2$PMe$_3$][Fe(CO)(NO)PMe$_3$]$^+$).

Synthesis of (μ-depdt)[(Fe(CO)$_2$PMe$_3$]$_2$PF$_6$ (2_{ox}-Et$_2$). Addition of a cold (−78 °C), CH_2Cl_2 solution of **2-Et$_2$** (0.054 g, 0.10 mmol) to a dry ice cooled solution of [Fc][PF$_6$] (0.033 g, 0.10 mmol) resulted in immediate color change from red to purple red. The reaction was stirred for 10 min and then warmed to −42 °C. Addition of precooled hexane formed purple/red precipitates which were isolated and washed with cold hexane. Yield 0.49 mg (87%). X-ray quality crystals were obtained by transferring 5 mL of a CH_2Cl_2 solution to a 12 mm diameter glass tube which was layered with pentane/diethyl ether mixed solution (2:1) and capped with a rubber septum. This was then stored in a Dewar flask filled halfway with ethylene glycol/dry ice and the rest of the way with crushed dry ice. Crystals grew after two weeks. IR (cm^{-1}, in CH_2Cl_2): ν(CO) 2041 (s), 2005 (s) 1993 (sh), 1874 (w). ESI-MS+ (CH_2Cl_2): m/z = 537.98 ((μ-depdt)[(Fe(CO)$_2$PMe$_3$]$_2$$^+$).

Computational Studies. All calculations reported were performed using the Gaussian 09 software suite[63] with a tight SCF convergence criteria of 10^{-8}. In all cases, the Cartesian coordinates of the crystallographic structures were utilized as the starting guess of the calculated structures for optimizations. Subsequent to each optimization, a frequency calculation was performed to ascertain a stable structure via the absence of imaginary frequencies. All results reported herein were calculated with a B3LYP functional[43,44] and a mixed basis set comprised of the SDD ECP parameters on Fe,[64−67] 6-311G on H,[64−67] and 6-311++G(d,p) on all other atoms.[64−67] Geometric parameters and molecular orbitals were obtained from the results of the geometry optimizations and visualized in the Ampac Graphical User Interface (AGUI) program,[68] and calculated infrared frequencies and APT populations were reported from the results of the frequency calculation. All reported vibrational frequencies have been scaled by a factor of 0.9679 as is typical for B3LYP with mainly Pople basis sets.[69] Molecular orbitals were plotted in AGUI at an isosurface value of 0.025 and spin densities at isosurface values of 0.001 and 0.005. The percent contribution by atom in the FMOs shown in Figures 9 and 10 were determined by squaring the atomic orbital coefficients of the renormalized molecular orbitals. All EPR parameters were quantum chemically evaluated starting from the geometry optimized structures of **2_{ox}-Me$_2$** and **2_{ox}-Et$_2$**. The calculations were performed using ORCA[42] on the DFT level of theory in combination with the B3LYP functional[43,44] and the IGLO-III basis set.[45]

■ ASSOCIATED CONTENT

Ⓢ Supporting Information

X-ray crystallographic data (CIF) from the structure determinations, full listing of metric parameters of complex **2-Et$_2$**, **2_{NO}-Me$_2$**, **2_{NO}-Et$_2$**, and **2_{ox}-Et$_2$**. Solid-state ATR-IR spectra of complexes **1-Me$_2$**, **1-Et$_2$**, **2-Me$_2$**, and **2-Et$_2$**. Spin density plots of **2_{ox}-Me$_2$** and **2_{ox}-Et$_2$**. SHFC parameters of complexes **2_{ox}-Me$_2$** and **2_{ox}-Et$_2$**. This material is available free of charge via the Internet at http://pubs.acs.org.

■ AUTHOR INFORMATION

Corresponding Author

wolfgang.lubitz@cec.mpg.de; cpopescu@ursinus.edu; hall@mail.chem.tamu.edu; marcetta@mail.chem.tamu.edu

Notes

The authors declare no competing financial interest.

■ ACKNOWLEDGMENTS

We acknowledge financial support from the National Science Foundation (CHE-0910679 to MYD, CHE-0956779 to CVP, and CHE-0910552 to MBH) and the R. A. Welch Foundation (A-0924 to MYD and A-0648 to MBH), and the EU/Energy Network Project SOLAR-H2 (FP7 contract 212508), and Max Planck Society (to OFE, ER, WL). OFE, ER, WL thank to Dr. William Ames (MPI Muelheim) for valuable discussions about ORCA, Dr. Stephen Sproules (University of Manchester) for help with the oxidation of the EPR samples, and Gudrun Klihm for technical assistance. The X-ray diffractometers, small angle scattering instrumentation and crystallographic computing systems in the X-ray Diffraction Laboratory at the Department of Chemistry, Texas A & M University, were purchased with funds provided by the National Science Foundation (CHE-9807975, CHE-0079822 and CHE-0215838).

■ REFERENCES

(1) Nicolet, Y.; Lemon, B. J.; Fontecilla-Camps, J. C.; Peters, J. W. *Trends Biochem. Sci.* **2000**, *25*, 138−143.

(2) Peters, J. W.; Lanzilotta, W. N.; Lemon, B. J.; Seefeldt, L. C. *Science* **1998**, *280*, 1853−1858.

(3) Darensbourg, M. Y.; Lyon, E. J.; Zhao, X.; Georgakaki, I. P. *Proc. Natl. Acad. Sci. U.S.A.* **2003**, *100*, 3683−3688.

(4) Fontecilla-Camps, J. C.; Volbeda, A.; Cavazza, C.; Nicolet, Y. *Chem. Rev.* **2007**, *107*, 4273−4303.

(5) Silakov, A.; Wenk, B.; Reijerse, E.; Lubitz, W. *Phys. Chem. Chem. Phys.* **2009**, *11*, 6592−6599.

(6) Knörzer, P.; Silakov, A.; Foster, C. E.; Armstrong, F. A.; Lubitz, W.; Happe, T. *J. Biol. Chem.* **2012**, *287*, 1489−1499.

(7) Vincent, K. A.; Parkin, A.; Armstrong, F. A. *Chem. Rev.* **2007**, *107*, 4366−4413.

(8) Tard, C.; Pickett, J. C. *Chem. Rev.* **2009**, *109*, 2245−2274.

(9) (a) Barton, B. E.; Rauchfuss, T. B. *Inorg. Chem.* **2008**, *47*, 2261−2263. (b) Olsen, M. T.; Rauchfuss, T. B.; Wilson, S. R. *J. Am. Chem. Soc.* **2010**, *132*, 17733−17740.

(10) (a) Lyon, E. J.; Georgakaki, I. P.; Reibenspies, J. H.; Darensbourg, M. Y. *Angew. Chem., Int. Ed.* **1999**, *38*, 3178−3180. (b) Lyon, E. J.; Georgakaki, I. P.; Reibenspies, J. H.; Darensbourg, M. Y. *J. Am. Chem. Soc.* **2001**, *123*, 3268−3278.
(11) (a) Le Cloirec, A.; Best, S. P.; Borg, S.; Davies, S. C.; Evans, D. J.; Hughes, D. L.; Pickett, C. J. *Chem. Commun.* **1999**, 2285−2286. (b) Jablonskytė, A.; Wright, J. A.; Pickett, C. J. *Dalton Trans.* **2010**, *39*, 3026−3034.
(12) (a) Schmidt, M.; Contakes, S. M.; Rauchfuss, T. B. *J. Am. Chem. Soc.* **1999**, *121*, 9736−9737. (b) Lawrence, J. D.; Li, H.; Rauchfuss, T. B.; Benard, M.; Rohmer, M. *Angew. Chem., Int. Ed.* **2001**, *113*, 1818−1821.
(13) Tard, C.; Liu., X.; Ibrahim, S. K.; Bruschi, M.; De Gioia, L.; Davies, S.; Yang, X.; Wang, L-S; Sawers, G.; Pickett, C. J. *Nature* **2005**, *434*, 610−613.
(14) Camara, J. M.; Rauchfuss, T. B. *Nature Chem.* **2012**, *4*, 26−30.
(15) Tye, J. W.; Hall, M. B.; Darensbourg, M. Y. *Inorg. Chem.* **2006**, *45*, 1552−1559.
(16) Helm, M. L.; Stewart, M. P.; Bullock, R. M.; DuBois, M. R.; DuBois, D. L. *Science* **2011**, *333*, 863−866.
(17) Nicolet, Y.; De Lacey, A. L.; Vernède, X.; Fernandez, V. M.; Hatchikian, C. E.; Fontecilla-Camps, J. C. *J. Am. Chem. Soc.* **2001**, *123*, 1596−1601.
(18) Liu, T.; Darensbourg, M. Y. *J. Am. Chem. Soc.* **2007**, *129*, 7008−7009.
(19) Justice, A. K.; Rauchfuss, T. B.; Wilson, S. R. *Angew. Chem., Int. Ed.* **2007**, *46*, 6152−6154.
(20) Singleton, M. L.; Bhuvanesh, N.; Reibenspies, J. H.; Darensbourg, M. Y. *Angew. Chem., Int. Ed.* **2008**, *47*, 9492−9495.
(21) Cheah, M. H.; Tard, C.; Borg, S. J.; Liu, X.; Ibrahim, S. K.; Pickett, C. J.; Best, S. P. *J. Am. Chem. Soc.* **2007**, *129*, 11085−11092.
(22) Siegbahn, P. E. M.; Tye, J. W.; Hall, M. B. *Chem. Rev.* **2007**, *107*, 4414−4435.
(23) Borg, S. J.; Tye, J. W.; Hall, M. B.; Best, S. P. *Inorg. Chem.* **2007**, *46*, 384−394.
(24) Gordon, J. C.; Kubas, G. J. *Organometallics* **2010**, *29*, 4682−4701.
(25) (a) Liu, T; Chen, S.; O'Hagan, M. J.; Bullock, R. M.; DuBois, M. R.; DuBois, D. L. *J. Am. Chem. Soc.* **2012**, *134*, 6257−6272. (b) Henry, R. M.; Shoemaker, R. K.; DuBois, D. L.; DuBois, M. R. *J. Am. Chem. Soc.* **2006**, *128*, 3002−3010.
(26) Felton, G. A. N.; Mebi, C. A.; Petro, B. J.; Vannucci, A. K.; Evans, D. H.; Glass, R. S.; Lichtenberger, D. L. *J. Organomet. Chem.* **2009**, *694*, 2681−2699.
(27) Vijaikanth, V.; Capon, J. F.; Gloaguen, F.; Schollhammer, P.; Talarmin, J. *Electrochem. Commun.* **2005**, *7*, 427.
(28) Na, Y.; Wang, M.; Pan, J. X.; Zhang, P.; Åkermark, B.; Sun, L. C. *Inorg. Chem.* **2008**, *47*, 2805−2810.
(29) Ekstrom, J.; Abrahamsson, M.; Olson, C.; Bergquist, J.; Kaynak, F. B.; Eriksson, L.; Licheng, S. C.; Becker, H. C.; Åkermark, B.; Hammarstrom, L.; Ott, S. *Dalton Trans.* **2006**, 4599−4606.
(30) Olsen, M. T.; Bruschi, M.; De Gioia, L.; Rauchfuss, T. B.; Wilson, S. R. *J. Am. Chem. Soc.* **2008**, *130*, 12021−12030.
(31) Popescu, C. V.; Stoian, S. A.; Erdem, O. E.; Hsieh, C.-H.; Singleton, M. L.; Casuras, A.; Reijerse, E. J.; Darensbourg, M. Y.; Lubitz, W. Manuscript in preparation.
(32) Singleton, M. L.; Jenkins, R. M.; Klemashevich, C. L.; Darensbourg, M. Y. *C. R. Chim.* **2008**, *11*, 861−874.
(33) Addison, A. W.; Rao, T. N.; Reedijk, J.; Van Rijn, J.; Verschoor, G. C. *J. Chem. Soc., Dalton Trans.* **1984**, 1349−1356.
(34) Chen, J.; Vannucci, A. K.; Mebi, C. A.; Okumura, N.; Borowski, S. C.; Swenson, M.; Lockett, L. T.; Evans, D. H.; Glass, R. S.; Lichtenberger, D. L. *Organometallics* **2010**, *29*, 5330−5340.
(35) Thomas, C. M.; Darensbourg, M. Y.; Hall, M. B. *J. Biol. Inorg. Chem.* **2007**, *101*, 1752−1757.
(36) Enemark, J. H.; Feltham, R. D. *Coord. Chem. Rev.* **1974**, *13*, 339−406.
(37) Conradie, J.; Hopmann, K. H.; Ghosh, A. *J. Phys. Chem. B* **2010**, *114*, 8517−8524.
(38) Hopmann, K. H.; Noodleman, L.; Ghosh, A. *Chem.—Eur. J.* **2010**, *16*, 10397−10408.
(39) Hopmann, K. H.; Ghosh, A.; Noodleman, L. *Inorg. Chem.* **2009**, *48*, 9155−9165.
(40) Hopmann, K. H.; Conradie, J.; Ghosh, A. *J. Phys. Chem. B* **2009**, *113*, 10540−10547.
(41) Ye, S.; Neese, F. *J. Am. Chem. Soc.* **2010**, *132*, 3646−3647.
(42) Neese, F. *Wiley Interdiscip. Rev.-Comput. Mol. Sci.* **2012**, *2*, 73−78.
(43) Lee, C. T.; Yang, W. T.; Parr, R. G. *Phys. Rev. B* **1988**, *37*, 785−789.
(44) Becke, A. D. *J. Chem. Phys.* **1993**, *98*, 5648−5652.
(45) Kutzelnigg, W., Fleischer, U., Schindler, M. Springer Verlag: Berlin, Heidelberg, 1991; Vol. *213*, pp 165−262.
(46) Dmitriev, Yu. A. *J. Low Temp. Phys.* **2005**, *139*, 541−549.
(47) Zhao, X.; Georgakaki, I. P.; Miller, M. L.; Yarbrough, J. C.; Darensbourg, M. Y. *J. Am. Chem. Soc.* **2011**, *123*, 9710−9711.
(48) Pereira, A. S.; Tavares, P.; Moura, J. J. G. M.; Huynh, B. H. *J. Am. Chem. Soc.* **2001**, *123*, 2771−2782.
(49) Popescu, C. V. Ph.D. Thesis, Department of Chemistry, Carnegie Mellon University, 2000.
(50) Popescu, C. V.; Münck, E. *J. Am. Chem. Soc.* **1999**, *121*, 7877−7884.
(51) Parish, R. V. *The Organometallic Chemistry of Iron*; Academic Press: New York, 1978; Vol. *1*, pp 175−211.
(52) Gütlich, P.; Bill, E.; Trautwein, A. X. *Mössbauer Spectroscopy and Transition Metal Chemistry*; Springer Verlag: Berlin, 2011.
(53) Jablonskyte, A.; Wright, J. A.; Fairhurst, S. A.; Peck, J. N. T.; Ibrahim, S. K.; Oganesyan, V. S.; Pickett, C. J. *J. Am. Chem. Soc.* **2011**, *133*, 18606−18609.
(54) Mulder, D. W.; Boyd, E. S.; Sarma, R.; Lange, R. K.; Endrizzi, J. A.; Broderick, J. B.; Peters, J. W. *Nature* **2010**, *465*, 248−251.
(55) Reijerse, E.; Lendzian, F.; Isaacson, R.; Lubitz, W. *J. Magn. Reson.* **2012**, *214*, 237−243.
(56) Stoll, S.; Schweiger, A. *J. Magn. Reson.* **2006**, *178*, 42−55.
(57) *APEX2*, version 2009.7-0; Bruker AXS, Inc.: Madison, WI, 2007.
(58) *SAINTPLUS: Program for Reduction of Area Detector Data, version 6.63*; Bruker AXS Inc.: Madison, WI, 2007.
(59) Sheldrick, G. M. *SADABS: Program for Absorption Correction of Area Detector Frames*; Bruker AXS Inc.: Madison, WI, 2001.
(60) Sheldrick, G. M. *SHELXS-97: Program for Crystal Structure Solution*; Universität Göttingen: Göttingen, Germany, 1997.
(61) Sheldrick, G. M. *SHELXL-97: Program for Crystal Structure Refinement*; Universität Göttingen: Göttingen, Germany, 1997.
(62) Macrae, C. F.; Edgington, P. R.; McCabe, P.; Pidcock, E.; Shields, G. P.; Taylor, R.; Towler, M.; van de Streek, J. *J. Appl. Crytsallogr.* **2006**, *39*, 453−457.
(63) Gaussian 09, Revision A.1: Frisch, M. J.; Trucks, G. W.; Schlegel, H. B.; Scuseria, G. E.; Robb, M. A.; Cheeseman, J. R.; Scalmani, G.; Barone, V.; Mennucci, B.; Petersson, G. A.; Nakatsuji, H.; Caricato, M.; Li, X.; Hratchian, H. P.; Izmaylov, A. F.; Bloino, J.; Zheng, G.; Sonnenberg, J. L.; Hada, M.; Ehara, M.; Toyota, K.; Fukuda, R.; Hasegawa, J.; Ishida, M.; Nakajima, T.; Honda, Y.; Kitao, O.; Nakai, H.; Vreven, T.; Montgomery, J. A., Jr.; Peralta, J. E.; Ogliaro, F.; Bearpark, M.; Heyd, J. J.; Brothers, E.; Kudin, K. N.; Staroverov, V. N.; Kobayashi, R.; Normand, J.; Raghavachari, K.; Rendell, A.; Burant, J. C.; Iyengar, S. S.; Tomasi, J.; Cossi, M.; Rega, N.; Millam, N. J.; Klene, M.; Knox, J. E.; Cross, J. B.; Bakken, V.; Adamo, C.; Jaramillo, J.; Gomperts, R.; Stratmann, R. E.; Yazyev, O.; Austin, A. J.; Cammi, R.; Pomelli, C.; Ochterski, J. W.; Martin, R. L.; Morokuma, K.; Zakrzewski, V. G.; Voth, G. A.; Salvador, P.; Dannenberg, J. J.; Dapprich, S.; Daniels, A. D.; Farkas, Ö.; Foresman, J. B.; Ortiz, J. V.; Cioslowski, J.; Fox, D. J. Gaussian, Inc., Wallingford CT, 2009.
(64) Krishnan, R.; Binkley, J. S.; Seeger, R.; Pople, J. A. *J. Chem. Phys.* **1980**, *72*, 650−654.
(65) Wachters, A. J. H. *J. Chem. Phys.* **1970**, *52*, 1033−1036.
(66) Hay, P. J. *J. Chem. Phys.* **1977**, *66*, 4377−4384.

(67) Raghavachari, K.; Trucks, G. W. *J. Chem. Phys.* **1989**, *91*, 1062–1065.

(68) AMPAC 9, Semichem, Inc., 12456 W 62nd Terrace, Suite D, Shawnee, KS 66216, 1992–2008.

(69) Andersson, M. P.; Uvdal, P. *J. Phys. Chem. A* **2005**, *109*, 2937–2941.